



Large-Eddy Simulations with remeshed Vortex methods: An Assessment and Calibration of Subgrid-Scale Models

Marthe de Crouy-Chanel, Chloé Mimeau, Iraj Mortazavi, Alessandro
Mariotti, Maria Vittoria Salvetti

► To cite this version:

Marthe de Crouy-Chanel, Chloé Mimeau, Iraj Mortazavi, Alessandro Mariotti, Maria Vittoria Salvetti.
Large-Eddy Simulations with remeshed Vortex methods: An Assessment and Calibration of Subgrid-Scale Models. *Computers and Fluids*, 2024, 277, pp.106287. 10.1016/j.compfluid.2024.106287 . hal-04582176

HAL Id: hal-04582176

<https://hal.science/hal-04582176>

Submitted on 21 May 2024

HAL is a multi-disciplinary open access archive for the deposit and dissemination of scientific research documents, whether they are published or not. The documents may come from teaching and research institutions in France or abroad, or from public or private research centers.

L'archive ouverte pluridisciplinaire **HAL**, est destinée au dépôt et à la diffusion de documents scientifiques de niveau recherche, publiés ou non, émanant des établissements d'enseignement et de recherche français ou étrangers, des laboratoires publics ou privés.

Large-Eddy Simulations with remeshed Vortex methods: An Assessment and Calibration of Subgrid-Scale Models

Marthe de Crouy-Chanel^{a,*}, Chloé Mimeau^a, Iraj Mortazavi^a, Alessandro Mariotti^b, Maria Vittoria Salvetti^b

^a*Laboratoire M2N, Conservatoire national des arts et métiers,
2 rue Conté, 75003 Paris, France*

^b*Dipartimento di Ingegneria Civile e Industriale, Università di Pisa,
Largo Lucio Lazzarino 2, 56122 Pisa, Italia*

Abstract

This study assesses various subgrid-scale models within the framework of Large Eddy Simulation (LES) using a remeshed Vortex method (RVM). RVM is a semi-Lagrangian method discretizing the vorticity-velocity Navier-Stokes equations that has proven to be a stable and less dissipative alternative to more classical Eulerian methods. The subgrid-scale models are first tested on the well-known Taylor-Green Vortex case at $Re = 5000$. Notably, the Variational Multiscale (VMS) variant of the Smagorinsky model and the Spectral Vanishing Viscosity (SVV) approaches emerge as the best-suited to the RVM, as they add diffusion to only the smallest resolved vorticity scales. Then, a stochastic uncertainty quantification analysis is conducted for both selected models, and the model coefficients are calibrated against direct numerical simulation. These coefficients are then applied to additional cases (different regimes, grid resolutions and test cases), showing the robustness of the calibration within the RVM-LES framework.

Keywords: Remeshed Vortex methods, Large Eddy Simulation, Variational Multiscale, Spectral Vanishing Viscosity, Uncertainty Quantification

*Corresponding author

Email address: marthe.de-crouy-chanel@lecnam.net (Marthe de Crouy-Chanel)

1. Introduction

Vortex methods [1, 2] are particle methods based on the vorticity-velocity ($\omega - \mathbf{u}$) formulation of the Navier-Stokes equations. They discretize the vorticity field on numerical particles following the flow dynamics in a Lagrangian way. In this work, we focus on remeshed Vortex methods (RVM), which can be seen as the semi-Lagrangian, or hybrid, variant of these approaches. In RVM, particles are repositioned or "remeshed" on a fixed grid after being advected [3]. This remeshing step enables the introduction of Eulerian methods in an initially Lagrangian algorithm, which allows to tackle the diffusion step and the Poisson equation in a more efficient way than in the purely Lagrangian approach [4]. In particular, Cartesian grids allow the use of a Fourier-based Poisson solver, reducing the computational cost compared to direct summation, despite the challenging treatment of boundary conditions inherent to such approaches.

Among the advantages of this type of approach one can first cite the absence of a CFL condition constraining the advection time step to the grid size, thanks to the Lagrangian transport of vorticity, then the low dispersivity and diffusivity when compared with non-spectral Eulerian methods (see [5] for a detailed comparison with the Lattice Boltzmann Method) and a similar accuracy to pseudo-spectral methods [6, 7]. This method thus demonstrates the advantage of hybridization between Lagrangian and Eulerian schemes, and because of its low diffusivity property, represents a good candidate to perform large eddy simulations (LES). Furthermore, RVM has the advantage of using vorticity as the principal variable instead of velocity. Indeed, vorticity dynamics plays a crucial role in turbulence; hence, having direct access to this field provides an advantage over the classical velocity-pressure formulation. For instance, by using the vorticity-velocity formulation in a purely Eulerian context, Tenaud *et al.* [8] and, more recently, Whitehouse *et al.* [9] emphasize the benefit of the direct access to vorticity in turbulent flow modeling and the improved performance for low resolution compared to the traditional $\mathbf{u} - p$ formulation. On the other hand, RVM are currently limited to Cartesian grids, which can be a disadvantage when considering complex geometries but facilitates the implementation of high order grid-based methods and parallelization.

The issue of closure modeling in LES with RVM has been significantly less explored compared to classical velocity-based formulations. Before delving into the specifics of subgrid-scale modeling for RVM, it is pertinent to provide

a general introduction to subgrid-scale modelling in general. Subgrid-scale (SGS) models are classically sorted into two families [10]. Functional models, as, e.g., the widely used Smagorinsky model [11], aim to model the role of the missing small scales in the flow by introducing an artificial viscosity term. Their effect is purely dissipative and these models do not account for backscatter, which is usually considered negligible compared to the transfer of energy from large to small scales [12]. Common variants of the Smagorinsky model include the dynamic Smagorinsky model [13] and Variational Multiscale Approaches (VMS) [14], both relying on explicit filtering to optimize the artificial viscosity term provided by the Smagorinsky model. Structural models, on the other hand, aim to model directly the subgrid-scale tensor by approximating the effects of the filtering applied to the equations, through, e.g., Taylor expansions. One of the most well-known models from this family is the gradient model [15]. It is to be noted that although these models are the most accurate in *a priori* tests, they are usually not dissipative enough and require modifications (coupling with a functional model [16], clipping [17–20]...). For this reason, the classification into these two families is often arbitrary as most models are a combination of both approaches. For example, the well-known and widely used dynamic version of the Smagorinsky model [13, 21] is often classified as functional since it is a variation of the Smagorinsky model but uses structural assumptions for its parameter computation procedure.

Approaches such as implicit Large eddy simulation (ILES) and regularization techniques like Spectral Vanishing Viscosity (SVV) [22–29] are becoming more and more popular as alternatives to classical modeling (see recent comparisons in [30, 31]). Some authors [32] argue that regularization is all one needs when it comes to correcting under-resolved simulations of turbulence. Regularization techniques are based on the introduction of numerical viscosity into the smallest of the resolved scales; this can be done directly in Fourier space (SVV) or by modifying a finite difference operator to introduce numerical dissipation [33, 34]. The simplicity of these techniques makes them less expensive and easier to implement than classical LES models.

As previously said, works on subgrid-scale models in the vorticity-velocity formulation are rare, particularly when using a semi-Lagrangian numerical method like the present one. In the context of purely Lagrangian methods, Winckelmans *et al.* [35, 36] and Mansfield *et al.* [37, 38] have adapted the dynamic Smagorinsky model [13, 21, 39] for the vorticity-velocity Navier-Stokes equations. Another approach is the one from Cottet *et al.* [40, 41]

introducing a structural model in two dimensions by analyzing the truncation error that stems from the approximation of vorticity and velocity fields by the Vortex method. This model can be linked to the family of gradient models [15, 16, 42] and has been used in the context of "two-level" simulations of the Navier-Stokes equations in $\omega - \mathbf{u}$ formulation [43] where the velocity and vorticity are discretized at different grid sizes, coarser for velocity and finer for vorticity. This model is anisotropic and less diffusive than usual functional models. Recently Alvarez *et al.* [44] adapted this model to develop a dynamic subgrid-scale model of stretching effects in a purely Lagrangian approach.

Hybrid approaches using Lagrangian discretization for the small scales of the flow fields and Eulerian discretization for the large scales were explored and applied to decaying homogeneous isotropic turbulence and free jet flows by Kornev and Samarbakhsh [45–47]. In the same spirit, Stock *et al.* [48] performed large eddy simulations of rotorcraft wakes using a Lagrangian discretization in the wake region and an Eulerian discretization for the near-body region. The LES model used in the Lagrangian regions was the one proposed by Cottet [40].

In the context of a remeshed Vortex method, Cocle *et al.* [49] focused on SGS models from the Variational Multi-Scale (VMS) [14] family. These models aim to address the excessive dissipation of the largest scales observed in classical artificial viscosity models. This is achieved by applying artificial viscosity exclusively to the smallest of the resolved scales, necessitating an additional explicit small-scale filtering. This approach was recently used for high-fidelity LES of challenging flows [50].

The objective of this article is thus twofold: 1) investigate and compare various subgrid-scale models of different families on the same benchmark, adapting them to the RVM. Although some comparative studies of SGS models already exist for RVM [41, 49, 51], the present RVM algorithm differs in the method used to solve the Poisson equation and the diffusion; moreover, we consider models never investigated yet in this context, like the SVV regularization technique. 2) Once the best models selected, we evaluate the sensitivity to their parameters. Indeed, in LES, uncertainties arising from SGS modeling can interact in a complex manner with those related to the numerical discretization. Therefore, it is not guaranteed that model parameters calibrated for the classical velocity-based framework are suitable for the RVM as well. To evaluate the impact of model coefficients on the LES-RVM results, we adopt a stochastic approach based on the polynomial chaos expansion [52], that provides response surfaces of the LES output quantities

in the parameter space requiring only a limited number of simulations. This allows an affordable calibration of the model parameters against reference DNS data. The SGS models calibration is conducted for the classical test case of the Taylor-Green vortex [53]. The robustness of calibration to changes in Reynolds number, grid resolution, and flow configuration (with the decaying homogeneous isotropic turbulence test case) is finally investigated.

The paper is structured as follows: the RVM is described in section 2. The different subgrid-scale models under consideration in our study are presented in section 3. The test cases considered herein are presented in section 4. The comparison of the results given by the various SGS models for the Taylor-Green Vortex (TGV) at $Re = 5000$ is presented in sections 4.3 and 4.4, allowing us to select the two most suitable models in terms of accuracy and computational costs. The stochastic sensitivity procedure, together with its application to the parameters of the two selected models, is described in section 5. Finally, section 6 investigates on the robustness of the parameter calibration by changing the flow Reynolds number and configuration, as well as the LES grid resolution.

2. The remeshed Vortex method

2.1. Governing equations

From the vorticity field definition $\boldsymbol{\omega} := \nabla \times \mathbf{u}$, one obtains the vorticity-velocity formulation of the incompressible Navier-Stokes equations by applying the curl operator to the classical velocity-pressure formulation:

$$\begin{cases} \frac{\partial \boldsymbol{\omega}}{\partial t} + (\mathbf{u} \cdot \nabla) \boldsymbol{\omega} - (\boldsymbol{\omega} \cdot \nabla) \mathbf{u} = \frac{1}{Re} \Delta \boldsymbol{\omega} \\ -\Delta \mathbf{u} = \nabla \times \boldsymbol{\omega} \end{cases} \quad (2.1)$$

$$(2.2)$$

completed with initial and boundary conditions, where \mathbf{u} , $\boldsymbol{\omega}$ and Re denote respectively the velocity, the vorticity and the Reynolds number. The term $(\mathbf{u} \cdot \nabla) \boldsymbol{\omega}$ denotes the advection of the vorticity field $\boldsymbol{\omega}$ by velocity \mathbf{u} , and $(\boldsymbol{\omega} \cdot \nabla) \mathbf{u}$ represents the stretching term. The Poisson equation (2.2) allows to recover the velocity field from the vorticity field derived according to the relation $\nabla \times \boldsymbol{\omega} = \nabla \times \nabla \times \mathbf{u} = \nabla(\nabla \cdot \mathbf{u}) - \Delta \mathbf{u}$ and the incompressibility condition $\nabla \cdot \mathbf{u} = 0$.

2.2. Vortex methods

Vortex methods [1], by their Lagrangian nature, offer a natural discretization of the flow field governed by equations (2.1)-(2.2). More precisely, in such methods, the vorticity field is discretized on numerical particles p located at positions \mathbf{x}_p , and the vorticity value at a given point \mathbf{x} of the domain and a given time t is approximated as follows:

$$\boldsymbol{\omega}^h(\mathbf{x}, t) = \sum_p \alpha_p^h \xi_\varepsilon(\mathbf{x} - \mathbf{x}_p^h(t)). \quad (2.3)$$

where ξ_ε is a mollifier and α_p^h is the local circulation, defined as $\alpha_p^h = \int_{\mathbf{v}_p} \boldsymbol{\omega}^h d\mathbf{x} = \boldsymbol{\omega}_p^h \mathbf{v}_p$, with \mathbf{v}_p the volume of the particle. The advection step in equation (2.1) is solved in a Lagrangian way, by updating particles position \mathbf{x}_p^h and local circulation α_p^h through two ODEs:

$$\begin{cases} \frac{d\mathbf{x}_p^h}{dt} = \mathbf{u}^h(\mathbf{x}_p^h(t), t) \\ \frac{d\alpha_p^h}{dt} = 0 \end{cases} \quad (2.4)$$

Grid-free Vortex methods are by construction particularly adapted to model advective effects. However, they show some difficulties in modeling diffusion effects efficiently due to the necessity to control the spatial distribution of the particles [2]. To alleviate this limitation, studies on spatial adaptation procedures were developed for Vortex methods. In the present work, we consider hybrid Vortex methods, where an underlying grid is introduced to easily control the positions of the particles and thus to avoid the distortion of the particle distribution.

2.3. Hybrid Vortex methods

These methods are characterized by the use of both Lagrangian and Eulerian approaches to discretize the Navier-Stokes equations (2.1)-(2.2) (see for example [6, 54, 55]). This approach allows us to keep the strengths from both approaches.

The Lagrangian framework is used for the advection of the vorticity field, as described above, and the Eulerian framework allows the use of finite differences and spectral methods to tackle more efficiently the stretching, the diffusion, and the Poisson equation. The use of a grid also facilitates the implementation of boundary conditions and the coupling of Navier-Stokes

with other equations in the context of multiphysics problems. As we will see later, the implementation of spectral viscosity SGS models is particularly easy within this approach.

In the present approach, the resolution of the Navier-Stokes equations (2.1)-(2.2) is based on a fractional time-stepping algorithm. The latter consists in performing substeps in which the convective, the stretching, the diffusive effects as well as the Poisson equation are considered successively within one time step. More precisely, the advection is handled in a Lagrangian way, on particles, by solving the system of ODEs (2.4) and the other steps are solved by an Eulerian method on a Cartesian grid. The keystone of the method is the "remeshing" step, in other words, the regular distribution of the particles on the underlying Cartesian grid. The remeshing step has a double function: it prevents the distortion of the particle distribution, ensuring control of the distance between particles, and serves as a bridge between the two approaches. Indeed, the underlying grid on which the Lagrangian particles are interpolated during the remeshing step is the same as the one used for the Eulerian steps.

2.4. Remeshing

During the remeshing step, the particles are projected on an underlying mesh. This is done by using remeshing kernels, functions denoted Λ , that satisfy several conditions [56]: they preserve p moments: $\sum_{k \in \mathbb{Z}} k^\alpha \Lambda(x - k) = x^\alpha$ for $0 \leq \alpha \leq p$ and $x \in \mathbb{R}$, they satisfy an interpolation property $\Lambda(i) = \mathbb{1}_{i=0}$, they have compact support $[-S, S]$ with $S \in \mathbb{N}$, and they are of class \mathcal{C}^r , with $r \in \mathbb{N}$. We further restrict ourselves to a family of even piecewise polynomials in the interval $[i, i + 1]$. These conditions are enough to derive, given an order p and a regularity r , our remeshing kernels $\Lambda_{p,r}$.

In one dimension, the vorticity at a node i of the mesh is then obtained from the vorticity carried by the neighboring particles p as follows:

$$\omega_i(x) = \sum_p \omega_p(x) \Lambda\left(\frac{x_p - x_i}{h}\right). \quad (2.5)$$

where h is the grid step. In the following we will work with the kernel $\Lambda_{4,2}$ of

compact support $[-3, 3]$, also known as M'_6 , given by:

$$\Lambda_{4,2}(x) = \begin{cases} 1 - \frac{5}{4}|x|^2 - \frac{35}{12}|x|^3 + \frac{21}{4}|x|^4 - \frac{25}{12}|x|^5 & 0 \leq |x| < 1 \\ -4 + \frac{75}{4}|x| - \frac{245}{8}|x|^2 + \frac{545}{24}|x|^3 - \frac{63}{8}|x|^4 + \frac{25}{24}|x|^5 & 1 \leq |x| < 2 \\ 18 - \frac{153}{4}|x| + \frac{255}{8}|x|^2 - \frac{313}{24}|x|^3 + \frac{21}{8}|x|^4 - \frac{5}{24}|x|^5 & 2 \leq |x| < 3 \\ 0 & 3 \leq |x| \end{cases} \quad (2.6)$$

Figure 1 depicts how the vorticity carried by a particle is redistributed on the grid points located in the support of the remeshing kernel $\Lambda_{4,2}$, following the weights-distribution given by (2.6).

2.5. Numerical algorithm and implementation

The present work employs the in-house and research open source HySoP (HYbrid SimulatiOn with Particles) library¹, dedicated to solving fluid related problems using the RVM approach described previously. It is a Python parallel solver, interfaced with compiled languages such as Fortran and C++ [7]. The algorithm adopted in HySoP for this study makes use of the particle approach to solve advection and uses finite differences to solve the stretching part and fast Fourier transform (with FFTW) to solve the diffusion and the Poisson equations. The remeshing of the particles on the underlying Cartesian grid is performed using the $\Lambda_{4,2}$ remeshing kernel (2.6).

The operator splitting realized in the present fractional step algorithm is further decomposed by using a so-called directional Strang splitting where 1D advection-remeshing-stretching problems are successively solved, direction by direction. This directional splitting allows to reduce the computational effort compared to a tensorial approach since it reduces the multidimensional partial differential equations to a sum of one-dimensional problems. In particular, advection and remeshing are performed in the same step using a second-order Strang splitting procedure (the reader is referred to [7] for more details). Table 1 summarizes the different numerical methods used for each step of the fractional step algorithm. Step 1) "Solenoidal reprojection" allows ensuring that the vorticity is a solenoidal field (ie. $\nabla \times \boldsymbol{\omega} = 0$) by projecting $\boldsymbol{\omega}$ on the space of divergence-free fields (see Appendix A).

¹https://particle_methods.gricad-pages.univ-grenoble-alpes.fr/hysop-doc/

	Fractional steps	Time integration	Space discretization
1) Solenoidal reprojection	$\Delta\omega = \Delta\omega^* - \nabla(\nabla \cdot \omega^*)$	-	spectral method (FFTW) (grid)
2) Poisson equation	$\Delta\mathbf{u} = -\nabla \times \omega$	-	spectral method (FFTW) (grid)
3) Diffusion	$\partial_t \omega = \frac{1}{Re} \Delta \omega$	implicit Euler	spectral method (FFTW) (grid)
4) Strang splitting (directional)			
a) Advection	$\begin{cases} \partial_t \mathbf{x}_p &= \mathbf{u}(\mathbf{x}_p(t), t) \\ \partial_t \omega &= 0 \end{cases}$	RK2	Lagrangian (particles)
b) Remeshing	$\omega(\mathbf{x}) = \sum_p \omega_p(\mathbf{x}) \Lambda(\frac{\mathbf{x}_p - \mathbf{x}}{\Delta \mathbf{x}})$	-	$\Lambda_{4,2}$ kernel (particles to grid)
5) Stretching (directional)	$\partial_t \omega = (\omega \cdot \nabla) \mathbf{u}$	RK3	4 th order centered FD (grid)
6) Adaptive time step	$\Delta t(t)$	-	4 th order centered FD (grid)

Table 1: Summary of the algorithm defining the different steps of the solution of Navier-Stokes equations (2.1)-(2.2) in the present RVM approach.

Finally, step (6) concerns the computation of an adaptive time step $\Delta t(t)$. Indeed, one important strength of Vortex methods is the absence of a CFL condition constraining the advection time step depending on the grid size. Instead, we have the so-called LCFL condition (where the "L" stands for Lagrangian) where the time step now depends on the infinity norm of the velocity gradient:

$$\Delta t \leq \Delta t_{adv,1} = \frac{C_{LCFL}}{\|\nabla \mathbf{u}\|_\infty}, \quad (2.7)$$

and where the constant C_{LCFL} , called the LCFL number, must be lower or equal to 1 [56]. Under this condition, the remeshed Vortex method for the incompressible Euler equation was shown to converge quadratically [56]. This convergence order was observed numerically for the Navier-Stokes equations. In practice, one also sometimes computes:

$$\Delta t_{adv,2} = \frac{C_{LCFL}}{\|\boldsymbol{\omega}\|_\infty} \quad \text{and} \quad \Delta t_{adv,3} = \frac{C_{LCFL}}{\|\mathbf{S}\|_\infty}, \quad (2.8)$$

where \mathbf{S} is the strain tensor. Concerning the stretching equation, the stability of the time discretization is ensured by the condition [55]:

$$\Delta t \leq \Delta t_{stretch} = \frac{C_{stretch}}{\max_i \left(\sum_j \left| \frac{\partial u_i}{\partial x_j} \right| \right)} \quad (2.9)$$

where $C_{stretch}$ is a constant depending on the time-integration scheme. The diffusion, which is solved by a spectral method, does not constrain the time

step. The simulation time step Δt is thus adapted at each iteration k of the overall algorithm as follows:

$$\Delta t^k = \min(\Delta t_{adv,1}^k, \Delta t_{adv,2}^k, \Delta t_{adv,3}^k, \Delta t_{stretch}^k) \quad (2.10)$$

In practice, the advection stability is found to be the most restrictive and thus the one driving the evolution of the time step. In this study, C_{LCFL} is set to $\frac{1}{8}$.

3. Subgrid-scale modeling

To perform large eddy simulations, we write the filtered Navier-Stokes equations in their vorticity-velocity formulation:

$$\frac{\partial \bar{\omega}}{\partial t} + \nabla \cdot (\bar{\omega} \otimes \bar{\mathbf{u}} - \bar{\mathbf{u}} \otimes \bar{\omega}) = \frac{1}{Re} \Delta \bar{\mathbf{u}} - \nabla \cdot \mathbf{R} \quad (3.1)$$

with $\bar{\omega}$ and $\bar{\mathbf{u}}$ the resolved (filtered) velocity and vorticity fields and with

$$\mathbf{R} = (\overline{\omega \otimes \mathbf{u}} - \bar{\omega} \otimes \bar{\mathbf{u}}) - (\overline{\mathbf{u} \otimes \omega} - \bar{\mathbf{u}} \otimes \bar{\omega}) \quad (3.2)$$

the subgrid-scale vorticity stress tensor to be modeled. As the vorticity-velocity formulation has two non-linear terms, the SGS stress tensor is composed of two terms, respectively the advection and the stretching ones. As done in the majority of LES simulations, we do not explicitly apply filtering to the governing equations, rather we assume that this is implicitly done by the numerical discretization. In the following, the (implicitly) filtered fields will be represented without the bar notation to simplify the notations.

In the present work, we assess artificial viscosity models (the standard Smagorinsky model and its dynamic and variational multiscale variants), and structural models with the Vreman's gradient model [15]. We also consider the Spectral Vanishing Viscosity approach which is especially well suited to the present RVM algorithm. For all the SGS models implemented in HySoP (except SVV), the differential operators implied in these models are discretized on the Cartesian grid, with fourth-order finite differences.

3.1. Artificial viscosity models

In velocity-pressure formulation, artificial viscosity models usually write:

$$\tau_{SGS} = \nu_{SGS} (\nabla \mathbf{u} + (\nabla \mathbf{u})^T) \quad (3.3)$$

where τ_{SGS} models the subgrid viscosity stress tensor $\tau = \overline{\mathbf{u} \otimes \mathbf{u}} - \bar{\mathbf{u}} \otimes \bar{\mathbf{u}}$. One takes the rotational of the velocity-pressure Navier-Stokes equations with the above artificial viscosity model, leading to:

$$\begin{aligned}\nabla \times (\nabla \cdot \tau_{SGS}) &= \nabla \times (\nabla \cdot (\nu_{SGS}(\nabla \mathbf{u} + (\nabla \mathbf{u})^T))) \\ &= \nabla \times (\nu_{SGS} \nabla \cdot (\nabla \mathbf{u} + (\nabla \mathbf{u})^T)) \\ &\quad + \nabla \times (\nabla \nu_{SGS} \cdot (\nabla \mathbf{u} + (\nabla \mathbf{u})^T)).\end{aligned}\quad (3.4)$$

Smagorinsky model. The vorticity-velocity Smagorinsky model, used in [36, 37] consists in considering only the first term of (3.4), leading to an anti-symmetric term vanishing in regions of zero vorticity, properties needed to model accurately \mathbf{R} [57]. One thus obtains the following expression for $\mathbf{g} \approx \nabla \cdot \mathbf{R}$:

$$\mathbf{g} = \nabla \times (\nu_{SGS} \nabla \cdot (\nabla \mathbf{u} + (\nabla \mathbf{u})^T)) = \nabla \times (\nu_{SGS} \Delta \mathbf{u}) = -\nabla \times (\nu_{SGS} \nabla \times \boldsymbol{\omega}) \quad (3.5)$$

which is equivalent (see Appendix B) to:

$$\mathbf{g} = \nabla \cdot (\nu_{SGS} (\nabla \boldsymbol{\omega} - (\nabla \boldsymbol{\omega})^T)) \quad (3.6)$$

Therefore:

$$\mathbf{R}_{SGS} = \nu_{SGS} (\nabla \boldsymbol{\omega} - (\nabla \boldsymbol{\omega})^T) \quad (3.7)$$

with ν_{SGS} given by the classical Smagorinsky model, that is:

$$\nu_{SGS} = (C_S \Delta)^2 |\mathbf{S}| \quad (3.8)$$

where C_S is a coefficient to be a-priori assigned, Δ the LES filter size, $\mathbf{S} = \frac{1}{2}(\nabla \mathbf{u} + (\nabla \mathbf{u})^T)$ and $|\mathbf{S}| = \sqrt{2 \mathbf{S}_{ij} \mathbf{S}_{ij}}$ the magnitude of the strain tensor \mathbf{S} .

Dynamic model. The most common variant of the Smagorinsky model is the dynamic Smagorinsky model [13] that uses test-filtering to dynamically adapt the model's coefficient in time and space. The approach is based on a scale-similarity assumption and solves a least-square problem to find an optimal value of C_S . This model has been used in the context of purely Lagrangian Vortex methods [37, 38].

Following [37], we write

$$\ell_i = \widehat{\mathbf{u}_j \partial_j \boldsymbol{\omega}_i} - \widehat{\boldsymbol{\omega}_j \partial_j \mathbf{u}_i} - \widehat{\mathbf{u}_j} \partial_j \widehat{\boldsymbol{\omega}_i} + \widehat{\boldsymbol{\omega}_j} \partial_j \widehat{\mathbf{u}_i} \quad (3.9)$$

and

$$m = \nabla \cdot M \quad (3.10)$$

with

$$M = \hat{\Delta}^2 |\hat{\mathbf{S}}| (\nabla \hat{\boldsymbol{\omega}} - (\nabla \hat{\boldsymbol{\omega}})^T) - \hat{\alpha} \quad (3.11)$$

where $\hat{\Delta}$ denotes the test filter size, $\hat{\mathbf{S}} = \frac{1}{2}(\nabla \hat{\mathbf{u}} + (\nabla \hat{\mathbf{u}})^T)$ and

$$\alpha = \Delta^2 |\mathbf{S}| (\nabla \boldsymbol{\omega} - (\nabla \boldsymbol{\omega})^T) \quad (3.12)$$

leading to

$$C_S = \frac{\langle \ell_i m_i \rangle}{\langle m_i m_i \rangle} \quad (3.13)$$

where the brackets represent an averaging over homogeneous directions.

Variational multiscale models. Another variant of the Smagorinsky model is the variational multiscale (VMS) family of models. VMS models, introduced by Hughes *et al.* [14] and first applied to RVM in [49] aim to circumvent the excessive dissipation of the largest scales introduced by classical artificial viscosity models. This is done by applying the artificial viscosity only to the smallest of the resolved scales, thus requiring an additional explicit small-scale filtering (see figure 2). In particular, we will focus on the "complete-small" variant of this approach where the SGS viscosity ν_{SGS} is computed from the complete range of scales of the velocity fields, as opposed to "small-small" and "small-complete" approaches where ν_{SGS} is computed from the small scales of the velocity field (the "small-small" variant was tested in the present study and was found to be more expensive as it required an additional explicit small-scale filtering for both the $\boldsymbol{\omega}$ and the \mathbf{u} fields while not improving significantly the results). In the following, as there is no ambiguity with another VMS approach, we will denote the selected "complete-small" variant by "VMS Smagorinsky model" or "VMS-Smag model". Let f be some resolved field, we define, in Fourier space, the largest resolved scales of f by $\hat{f}(k) = \hat{G}(k)f(k)$ where \hat{G} is some test filter, and the smallest resolved scales f_S by $f_S = f - \hat{f}$. One therefore defines the VMS-Smag model by:

$$\mathbf{R}_{SGS} = \nu_{SGS} (\nabla \boldsymbol{\omega}_S - (\nabla \boldsymbol{\omega}_S)^T) \quad (3.14)$$

where $\boldsymbol{\omega}_S$ denotes the small scales of the resolved vorticity field and where the eddy viscosity ν_{SGS} is defined by eq. (3.8), from the complete range of scales of the velocity fields.

Filtering. In the following we will filter the large resolved scale using the filter presented in [58]. It is based on the stencil:

$$\hat{\mathbf{u}}^{(n)} = [(I - (-\delta_x^2/4)^n)(I - (-\delta_y^2/4)^n)(I - (-\delta_z^2/4)^n)] \mathbf{u} \quad (3.15)$$

where $\delta_x^2 f_{i,j,k} = f_{i+1,j,k} - 2f_{i,j,k} + f_{i-1,j,k}$. In Fourier space, the filtered field is then

$$\hat{\mathbf{u}}^{(n)}(\mathbf{k}) = G^n(\mathbf{k})\mathbf{u}(\mathbf{k}) = \mathcal{G}^n(k_x h_x) \mathcal{G}^n(k_y h_y) \mathcal{G}^n(k_z h_z) \mathbf{u}(\mathbf{k}) \quad (3.16)$$

with h the grid step and

$$\mathcal{G}^n(k) = (1 - \sin^{2n}(k/2)). \quad (3.17)$$

The small scales are then obtained as follows:

$$\mathbf{u}_S^{(n)} = \mathbf{u}(\mathbf{k}) - \hat{\mathbf{u}}^{(n)}(\mathbf{k}) = (1 - G^n(\mathbf{k}))\mathbf{u}(\mathbf{k}). \quad (3.18)$$

Figure 3 shows the evolution of $1 - \mathcal{G}^n$ with the wavenumber k for different values of n . In this work we performed all filtering operations in the Fourier space, taking advantage of the interfacing of the Hysop library with the Fortran FFTW library, already used to solve the diffusion and the Poisson equations (see Table 1). It has to be noticed that this type of filtering has the property of being also applicable in the physical space, under the condition of taking integer values of n , as done in [49] for a variant of the hybrid Vortex method.

3.2. A structural model: the clipped gradient model

Among structural models, which aim to directly model the subgrid-scale tensor, we explore the gradient model [15] based on a Taylor series expansion. It writes:

$$\mathbf{R}_g(i, j) = \frac{\Delta^2}{12} (\partial_k \boldsymbol{\omega}_i \partial_k \mathbf{u}_j - \partial_k \boldsymbol{\omega}_j \partial_k \mathbf{u}_i). \quad (3.19)$$

This model is well known for its good *a-priori* performances and its low cost, but we observed that it tends to overestimate back-scatter effects and leads to unstable simulations. We therefore propose to add the following clipping procedure:

$$\mathbf{R}_g^{clip}(i, j) = \frac{\Delta^2}{12} (\partial_k \boldsymbol{\omega}_i \partial_k \mathbf{u}_j - \partial_k \boldsymbol{\omega}_j \partial_k \mathbf{u}_i) \times \begin{cases} 1 & \text{if } \mathbf{R}_g(i, j)\Omega_{ij} < 0 \\ -1 & \text{otherwise} \end{cases} \quad (3.20)$$

where $\Omega_{ij} = \frac{1}{2}(\partial_j \omega_i - \partial_i \omega_j)$. In this clipping approach, we focus on the directions where the model leads to an energy transfer from the small to the large scales, inverting the sign of the model in those specific directions. In the velocity-pressure formulation, it corresponds to the directions where $\tau_{ij} S_{ij} > 0$ [59]. In our vorticity-velocity formulation, we consider the enstrophy-producing directions.

3.3. Spectral vanishing viscosity

Spectral vanishing viscosity (SVV) models were first introduced by [22–24] to regularize hyperbolic problems solved by spectral methods. They were then used for LES of Navier-Stokes [25–29]. Spectral vanishing viscosity approaches are a type of regulation of spectral methods that consists in adding progressively viscosity to the end of the spectrum, where non-physical oscillations may occur. The coarser scales remain untouched, which makes them similar to the VMS model presented previously. To further the analogy, we choose to use the same small-scale filtering for both VMS-Smag and SVV models (i.e. eq. (3.18)).

The two methods differ however in that the VMS-Smag model viscosity is computed from the whole resolved velocity field (cf eq. (3.8)) whereas in SVV, as detailed below, the viscosity is simply taken to be proportional to the cutoff scale. Furthermore, from a computational point of view, the SVV is directly integrated in the Fourier part of our solver whereas the VMS-Smag model (3.14) requires a new discretization operator (performed with finite differences in the present case).

In Fourier space, the modified diffusion operator writes:

$$\partial_t \hat{\omega} = -(k_x^2(1/Re + \nu_S(k_x)) + k_y^2(1/Re + \nu_S(k_y)) + k_z^2(1/Re + \nu_S(k_z)))\hat{\omega} \quad (3.21)$$

with the spectral viscosity ν_S given by the expression introduced by [24]:

$$\nu_s(k) = \begin{cases} 0 & \text{if } k < k_m \\ \nu_0 \exp \left[- \left(\frac{k_c - k}{k_m - k} \right)^2 \right] & \text{if } k_m \leq k \leq k_c \end{cases} \quad (3.22)$$

where k_c is the wavenumber at the cutoff scale. The SVV technique depends then on two parameters: the artificial viscosity intensity ν_0 and the cutoff wavenumber k_m from which the artificial viscosity is added.

In the present formulation, the SVV operator (3.21) is anisotropic. In our study, we consider mostly homogeneous and isotropic flows and we

Model	Small scale filter
Smag	none
VMS-Smag	\mathcal{G}^n
classical SVV	\mathcal{Q}_{SVV}
present SVV	$\mathcal{Q}_{SVV} \star \mathcal{G}^n$

Table 2: Summary of the different filters considered in the present study

found very little variation in the results between the present formulation and an isotropic operator (i.e. one that introduces the same viscosity for each direction). However, we believe that having a flexible operator with the ability to introduce a different viscosity amplitude at a different rate in each direction can be a useful feature for more complex flow configurations. As argued in [32], anisotropy can also be an asset to correct anisotropic errors due to numerical differentiation in the physical space.

As previously said, instead of using a cutoff at k_m , and to simplify the comparison with the other models and the following uncertainty quantification study, the filter used for the SVV operator is chosen to be the same as the one used for the VMS-Smag model:

$$\nu_s(k, h) = \nu_0 \exp \left[- \left(\frac{k_c - k}{k_m - k} \right)^2 \right] (1 - \mathcal{G}^n(kh)) =: \nu_0 \mathcal{Q}_{SVV}(k)(1 - \mathcal{G}^n(kh)) \quad (3.23)$$

with h the grid step. The evolution of ν_S with the wavenumber k is shown in figure 4 and compared to the one of the classical formulation (3.22). Table 2 presents a summary of the different filters presented above, showing the link between the VMS and SVV approaches. Indeed, the SVV approach can be seen as an anisotropic variant of the VMS-Smag model, with a different filter and a constant viscosity.

The SVV approach requires the definition of two parameters, namely k_m (or, in the present study, the order n of the explicit filter (3.23)) and ν_0 . In the literature, a scaling of the SVV viscosity ν_0 by $1/k_c$ (meaning that the SVV viscosity becomes negligible as the resolution increases) has been studied by [29] in the context of a LES of the turbulent wake around a cylinder. Other approaches consist in scaling the viscosity with the velocity field [26], the ratio of the Kolmogorov scale to the resolved scale [33] or using the artificial viscosity given by the Smagorinsky model [60]. In our context, since we are applying the SVV operator directly in the Fourier space, it is not

appropriate to scale the artificial viscosity with a quantity varying in space. In the following, we therefore study viscosities ν_0 of the form:

$$\nu_0 = \frac{C_{SVV}}{k_c} \quad (3.24)$$

where C_{SVV} is a coefficient to be set.

4. Test cases

4.1. Taylor-Green Vortex

The Taylor-Green vortex (TGV) [53] is an analytical periodic solution of the Navier-Stokes equations in a cubic box of length $L = 2\pi$ with initial vorticity given by:

$$\boldsymbol{\omega}(x, y, z, t = 0) = \begin{pmatrix} -U_\infty \cos(x) \sin(y) \sin(z) \\ -U_\infty \sin(x) \cos(y) \sin(z) \\ 2U_\infty \sin(x) \sin(y) \cos(z) \end{pmatrix} \quad (4.1)$$

All fields are discretized on a cubic grid with N points in each direction. The TGV is a common benchmark to test SGS models since it is representative of the phenomenon of large vortex breaking into smaller structures under the influence of vortex stretching. In this study, we consider the transitional and turbulent cases at $Re = 1600$, $Re = 3000$, $Re = 5000$, where the Reynolds number is defined as $Re = U_\infty L / \nu$, with ν the kinematic viscosity of the fluid. The case $Re = 1600$ is the most widely studied in the literature, however we found that in our RVM approach, no-model LES is enough to provide a good approximation of the flow, even at low resolution. Conversely, recent literature [33, 61, 62] has employed a Reynolds number of 5000. Notably, at such Re number and for the low resolutions we are considering, the simulation is unstable without a SGS model.

4.2. Decay of homogeneous isotropic turbulence

We consider another classical test case: the decay of homogeneous isotropic turbulence (HIT). The initial velocity and vorticity fields are obtained using the procedure described by Rogallo [63] in a cubic box of size $2\pi^3$ with a 512^3 grid resolution from the initial spectrum given by:

$$E_{init}(|\mathbf{k}|, 0) = 16\sqrt{2/\pi}k_f^{-5}|\mathbf{k}|^4e^{-2(|\mathbf{k}|/k_f)^2} \quad (4.2)$$

where here $k_f = 3$. The turbulence is then forced in Fourier space [64] with:

$$\partial_t \hat{\omega} = \frac{1_{[|\mathbf{k}| \leq k_f]}}{2 \sum_{|\mathbf{k}| \leq k_f} E(|\mathbf{k}|)} \hat{\omega} \quad (4.3)$$

Once a statistically steady flow has been reached, the turbulent state is interpolated on a coarser grid, used as the initial state for the LES. Two cases with different viscosities are explored. The Reynolds numbers based on the Taylor microscale and considered in the following are $Re_\lambda = 140$ and $Re_\lambda = 210$.

4.3. Comparison of model performances

The different models are first compared in the context of the TGV test case, at $Re = 5000$. The results are compared against those of a DNS conducted with the present RVM and a 768^3 grid resolution. For the purpose of comparison, the DNS enstrophy data are filtered on the same grid used for LES using a sharp cutoff filter. For the specific quantity of dissipation, the results are compared against available reference DNS at a higher resolution of 1280^3 from [33]. We start by comparing the LES results obtained with our RVM approach with those of a LES conducted with a purely Eulerian method. Figure 5 presents a comparison of the dimensionless-time history of kinetic energy dissipation of a 72^3 LES simulation with RVM and the standard Smagorinsky model with that obtained by Chapelier *et al.* [61], using high-order finite differences with the Smagorinsky model as well. The model coefficient for both simulations is $C_S = 0.172$. We observe in both cases a shift in the time evolution of kinetic energy dissipation but our method seems to better represent the peak of dissipation, demonstrating its low-diffusivity.

In figure 6, the time history of the kinetic energy E_k (*a*), the kinetic energy dissipation $-dE_k/dt$ (*b*), the enstrophy $\langle \boldsymbol{\omega} \cdot \boldsymbol{\omega} \rangle$ (*c*), and the energy spectrum at non-dimensional time $t = 8.5$ (*d*) are used to evaluate the different models by comparison to the non-filtered DNS results from [33] for the dissipation (*b*) and to the present DNS results for the other quantities (*a, c, d*).

The LES simulations are performed with $N_{LES} = 96$. The model coefficients used are the classical $C_S = 0.16$ for Smagorinsky and coefficients close to the ones suggested in [51] for VMS-Smag and in [29] for SVV ($C_S = 0.245$ and $n = 3$ and $C_{SVV} = 0.25$ and $n = 5$ respectively).

As can be seen, the no-model simulation (i.e. under-resolved simulation with no SGS model) is characterized by the classical pile up of energy at

the small scales and is unstable. In all cases, the introduction of a SGS model leads to stable simulations. The standard Smagorinsky seems to damp excessively the large scales, while energy pile up is still present at the smallest resolved scales (figure 6(d)). Moreover, the peak in dissipation occurs earlier than in DNS, and, consequently, the kinetic energy decay is more rapid in the first phase of the evolution. The gradient model gives results very similar to those obtained with the Smagorinsky model. It has to be noticed that the dynamic Smagorinsky model also behaves similarly to the Smagorinsky model, as shown in figure 7(a). This may be due to the considered test case. Indeed, in the absence of walls or strong inhomogeneities in the flow, the advantage of adapting the model coefficient in space is less visible. When observing the evolution of the dynamic coefficient in time (figure 7(b)), we find that it quickly stabilises to a constant coefficient close to the one used for the standard Smagorinsky model, namely $C_S = 0.16$. Finally, the SVV and VMS-Smag models give a kinetic energy spectrum in good agreement with the one obtained in DNS (figure 6(d)), thus confirming the benefit of introducing SGS viscosity only at the smallest resolved scales of the flow without adding dissipation to the largest scales. The SVV gives the best global agreement with DNS, in particular for the kinetic energy decay (figure 6(a)) and the energy spectrum (figure 6(d)).

4.4. Comparison of computational times

Table 3 compares the CPU-time per iteration for various models. This study was performed on sequential (non-parallel) runs of the TGV test case at $Re = 1600$ and $N_{LES} = 64$ over 2000 iterations, in order to have a stable baseline simulation with no SGS model. Indeed, the simulation of the TGV test case at $Re = 1600$ and $N_{LES} = 64$, with the RVM approach and without any SGS model, is stable and does not blow up. All simulations were performed on the same hardware (Xeon E5-2650L v3 1.8GHz). The CPU times are normalized by the no-model runtime.

As anticipated, all models imply an increase in computational time compared to the baseline simulation without any model. However, the impact is almost negligible when adopting the SVV approach, given that it does not require the introduction of a new term to be discretized but only a modification of the existing Fourier-based diffusion operator. The VMS Smagorinsky model requires a higher computational cost than the standard Smagorinsky due to the explicit filtering operation needed to separate the smallest resolved scales from the largest ones. However, the additional increase in computational time

Model	normalised averaged time per iteration
Smag	1.14
Dynamical Smag	1.81
VMS Smag	1.2
Gradient	1.19
SVV	1.02

Table 3: Time per iteration for LES simulations of TGV at $Re = 1600$ and $N_{LES} = 64$ normalised by the time per iteration for a no-model simulation.

is relatively minor, especially when considering the enhanced performance achieved compared with the standard Smagorinsky model (see figure 6). The dynamic Smagorinsky model is the least efficient in terms of computational costs. This can be attributed to the numerous filtering and derivative operations required by equations (3.9)-(3.13), particularly within the context of the vorticity-velocity formulation. Therefore, while our current implementation of the dynamic Smagorinsky model may benefit from optimization, we do not expect to be able to reduce the computational costs at the same level of that of the other considered models, due to the inherent required number of filtering operations and additional differential terms to be discretized.

Based on the simulation results and computational cost comparison, the VMS-Smag and the SVV models come out as the most adapted models in our framework. However, both SGS models involve a set of parameters that can or must be assigned a priori. The main ones are the model coefficients, C_S and C_{SVV} , which directly regulate the amount of SGS viscosity, and the order n of the filter in equations (3.17) and (3.23), which determines the range of the smallest resolved scales in which the SGS viscosity is introduced. While testing different values of these parameters in LES of the TGV case, we observed significant changes in the results even with a slight variation in the parameter values. To systematically study the sensitivity of both models to their parameters while keeping the number of needed simulations reasonable, an uncertainty quantification procedure is performed and presented in the following section.

5. Parameter sensitivity analysis

5.1. Uncertainty quantification procedure

We perform an uncertainty quantification study using the Polynomial Chaos Expansion (PCE) [52] to study the stochastic sensitivity of the results given by the VMS-Smag and the SVV models to their main parameters.

Uncertainty quantification is based on considering the model parameters as uncertain random variables. By assuming their PDFs, one can propagate those uncertainties and evaluate the sensitivity of the results to the variation of the parameters. PCE is based on modeling the response surface as a combination of polynomials in the considered variables. We choose a polynomial basis Ψ_p and write the response surface u as a function of the parameters y :

$$u(y) = \sum_{i=0}^{\infty} \hat{u}_i \Psi_i(y) \quad (5.1)$$

the coefficients \hat{u}_i are computed by

$$\hat{u}_i = \int u(y) \Psi_i(y) dy \quad (5.2)$$

To practically obtain the response surface, it is necessary to truncate the sum in equation (5.1). This finite limit L is here determined as follows:

$$L = \prod_{k=1}^M (P_k + 1) - 1 \quad (5.3)$$

where M is the number of uncertain variables considered in the problem and P_k is the highest polynomial order selected for the variable of index k .

Once the coefficients \hat{u}_i computed, the mean value and the variance of u can be computed as:

$$\mathbb{E}[u] = \hat{u}_0 \quad (5.4)$$

$$Var[u] \approx \sum_{i=0}^L \hat{u}_i^2 - \hat{u}_0^2 \quad (5.5)$$

The partial sensitivities, i.e. the contribution of each parameter (or combination of them) to the total variance, are evaluated through the partial variances [65]:

$$S_{i_1, i_2, \dots, i_S} = \int u_{i_1, i_2, \dots, i_S}^2 dy_{i_1} dy_{i_2} \dots = \sum_{p \in \mathcal{P}_{i_1, i_2, \dots}} \hat{u}_p^2 \quad (5.6)$$

n	1.8332	3.0000	4.5223	5.6891
C_S	0.23	0.3617	0.5335	0.6652
C_{SVV}	0.0187	0.0887	0.18	0.25

Table 4: Quadrature points used for the uncertainty quantification study performed for the VMS-Smag model (with parameters n and C_S) and for the SVV model (with parameters n and C_{SVV}).

In the present work, the uncertain parameters of the numerical simulations are the following: model coefficient C_S (eqs. (3.14) and (3.8)) and filter order n (eq. (3.17)) for the VMS-Smag model and model coefficient C_{SVV} (eq. (3.24)) and filter order n for the SVV approach (eq. (3.23)). We consider the following ranges of variation of the parameters $C_S \in [0.1949, 0.7]$, $C_{SVV} \in [0, 0.2685]$ and $n \in [1.5223, 6]$ and uniform input PDF within these ranges. These intervals were determined as follows: we started from the values recommended in the literature and we first checked whether the introduced SGS viscosity could be decreased while maintaining a stable simulation. For SVV, also for very low values of C_{SVV} the simulations were stable and, thus, the value proposed in the literature, $C_{SVV} = 0.25$, is the largest quadrature point in the considered interval. Conversely, for the VMS-Smag model, LES simulations became unstable for values of C_S slightly lower than the value recommended in the literature, $C_S = 0.23$; therefore, we also included significantly larger values in the C_S variation range. In the above intervals, a constant probability density function (PDF) is postulated because, among the traditionally employed distributions, it is the least informative, exhibiting the highest variance within specified intervals. We choose the Legendre polynomial family for the gPC expansion, which is the optimal one when dealing with uniform PDF distributions. For all the uncertainty parameters, the expansion in equation (5.1) is truncated to the third order ($P_k = 3$ for all k). Thus, four quadrature points are needed for each parameter, as summarized in table 4. Since we consider two parameters for each model ($M = 2$), we have $L = 15$ which corresponds to 16 simulations to be performed for each model. The polynomial chaos expansion was performed using the **Dakota** library².

Figure 8 shows the average absolute value of the polynomial coefficients obtained for the PCE in the case of the SVV and VMS-Smag models for

²<https://dakota.sandia.gov/>

each order of polynomial. As one can see, the average absolute values for coefficients associated to polynomial with order > 3 are about an order of magnitude smaller than the coefficients associated with polynomials of order 3. This justifies our choice in the truncation order.

5.2. Sensitivity to parameters for the VMS-Smagorinsky model

Figure 9 and 10 present the sensitivity analysis of the VMS-Smag model for the TGV test case at $Re = 5000$ with $N_{LES} = 96$. The impact of the two parameters is studied for three quantities of interest: kinetic energy dissipation (figures 9(a)(c)), enstrophy (figures 9(b)(d)) and kinetic energy spectrum at $t = 8.5$ (figure 10). In both figures 9 and 10, the probability density functions (PDFs) of each quantity are shown and compared with the DNS from [33] for dissipation and present DNS with $N_{DNS} = 768$ for the other quantities. The PDFs for the quantities of interest are visually represented through a color gradient, where each segment of the plot is shaded following the likelihood of the quantity falling within that specific range. Hence, the darkest part of the plot identifies where the analyzed quantities show the lowest variation. One observes a strong variability at the peak of enstrophy (figure 9(b)) and at the tail of the spectrum (figure 10(a)), where the model is the most active. In figures 9(c)-(d) and 10(b), the partial variances are plotted as a function of time for enstrophy and dissipation (figure 9) and of wavenumber for the spectrum (figure 10). They represent the relative sensitivity to each of the two parameters and to the interaction between those parameters. The impact of the interaction is always quite low, showing the independence of the two parameters. The model seems to be sensitive to both parameters and in regions of high variability, the coefficient C_S is the dominant one.

Figure 11 represents the computed polynomial chaos expansion interpolation of the relative ℓ^2 -error for enstrophy and kinetic energy spectrum obtained in LES compared with the 768^3 DNS. The error is represented as a function of coefficients C_S and n . The minima for the reconstructed response surfaces of the error for the energy spectrum and the enstrophy being close to each another, we identified the optimal values by taking their average. This led to $n = 6$ and $C_S = 0.41$.

5.3. Sensitivity to parameters for the SVV model

In a similar way, the PDFs and partial variances for kinetic energy dissipation, enstrophy (fig. 12), and kinetic energy spectrum at $t = 8.5$ (fig. 13)

are shown for the SVV model. The quantities of interest given by the LES with the SVV model show a lower variability than for the VMS-Smag model. The agreement with the reference DNS is generally good, i.e., except for the peaks of dissipation for which the DNS value stands lightly outside of the PDF. When considering the partial variances, we observe that the model is much more sensitive to the coefficient C_{SVV} than to the filter order n . This is also observed in figure 14, showing the relative ℓ^2 -error for enstrophy and kinetic energy spectrum compared with the DNS. The error does not vary much along the n axis. The two quantities show a local minimum in the same region, around $C_{SVV} = 0.1$ favoring small values of viscosity as observed in [27, 66]. Since the order of the filter was observed to be minor compared to that of the coefficient value and since the optimal value of the filter order is not clear, for further comparisons with VMS-Smag, we chose $n = 6$.

6. Simulations with calibrated coefficients

6.1. Taylor-Green Vortex

The uncertainty quantification conducted on the TGV test case at $Re = 5000$ with a resolution of $N_{LES} = 96$ revealed specific regions in the space of the parameters involved in the VMS-Smag and SVV models, corresponding to low errors in the quantities of interest compared with DNS. This allowed us to identify two "optimal" couples of parameters $(C_S, n) = (0.41, 6)$ and $(C_{SVV}, n) = (0.1, 6)$ for the two SGS models. To evaluate the robustness of this calibration, we assess the results obtained in LES with the two SGS models and the calibrated parameters, for various resolutions and Reynolds numbers.

Figure 15 shows the kinetic energy spectra for $Re = 1600, 3000$ and 5000 (along rows) and $N_{LES} = 64, 96$ and 128 (along columns). We recall that the calibration was performed for the $Re = 5000$ and $N_{LES} = 96$ case (figure 15(h)). A comparison with DNS is shown (with $N_{DNS} = 512$ at $Re = 1600$ and $N_{DNS} = 768$ otherwise). For every configuration, the no-model case overestimates the energy in the small scales and over-dissipates the large scales. The VMS-Smag and SVV models with the "optimal" parameters show a very good agreement with the reference spectra until the cutoff.

Figure 16 shows the time history of the enstrophy in the following three configurations: $(Re = 1600, N_{LES} = 64)$, $(Re = 3000, N_{LES} = 64)$ and $(Re = 5000, N_{LES} = 96)$. A comparison with filtered DNS is shown (with $N_{DNS} = 512$ at $Re = 1600$ and $N_{LES} = 768$ otherwise). The same conclusions

as before hold, with a slightly better performance in the peak and the decay of turbulence for SVV, the maximum value of enstrophy for SVV having a relative error with the peak of enstrophy for the filtered DNS of 5%, 2% and 0.9% for $Re = 1600, 3000$ and 5000 respectively (although the peak is shifted for $Re = 5000$).

Figure 17 shows the time history of kinetic energy dissipation in the configuration for $Re = 1600, 3000$ and 5000 (along rows) and $N_{LES} = 64, 96$ and 128 (along columns). A comparison with non-filtered DNS is shown (with $N_{DNS} = 512$ for $Re = 1600$ and $N_{LES} = 768$ for $Re = 3000$ and the reference DNS from [33] for $Re = 5000$). It has to be noticed that this quantity was not included in our optimization procedure. Interestingly, the same conclusions as for enstrophy and kinetic energy spectra hold for the dissipation: the VMS-Smag is slightly more dissipative in the coarser resolutions, however, contrary to enstrophy, it shows a better agreement with the DNS in the higher resolutions. The "double bump" observed near the peak of dissipation has already been observed for intermediate resolutions in other DNS performed with RVM (see for example Figure 9 of [5]) and is certainly a feature due to the remeshing kernel order as shown in [7] (section 3.2.8). In summary, these results indicate that the calibrated parameter values for both the VMS-Smag and SVV SGS models perform well even for Reynolds numbers, grid resolutions and physical quantities different from those they were initially optimized for. Finally, figure 18 depicts the qualitative performance of the VMS-Smag and SVV models for the TGV test case at $Re = 5000$ with $N_{LES} = 128$. The flow structures drawn by the streamwise velocity component u_x at the slice $x = \pi/8$ are compared with the DNS structures with $N_{DNS} = 768$. The no-model case is under-resolved and although it manages to capture the macro scales of the flow, it exhibits spurious oscillations. The structures for the VMS-Smag and SVV models confirm the previous results by showing a good qualitative agreement with DNS, with the VMS-Smag model being slightly more diffusive.

6.2. Decay of homogeneous isotropic turbulence (HIT)

The SVV and VMS-Smag models together with their "optimal" parameter values are then tested for a different test case. First, we aim to assess whether the model coefficients calibrated for the TGV case yield accurate results for a different flow configuration as well. As in the case of the TGV, we also investigate whether the parameter calibration is robust to changes in numerical resolution or Reynolds number. To these aims, we considered

another classical test case: the decay of homogeneous isotropic turbulence (HIT), previously described in section 4.

The VMS-Smag model with the coefficients calibrated for the TGV case, namely $(C_S, n) = (0.41, 6)$, was found to give satisfactory results also for HIT without any adaptation, and the results will be compared against DNS in the following. Conversely, we found that the SVV SGS model with the previously calibrated parameters does not provide enough dissipation, yielding inaccurate results for all Reynolds numbers and resolutions studied. A new sensitivity analysis was then conducted with SVV for the case $Re_\lambda = 210$ and $N_{LES} = 64$. Figure 19 shows the response surfaces in the parameter space of the error compared with DNS with $N_{DNS} = 256$ for enstrophy and kinetic energy spectrum. It can be seen that the minimum of the error is around $C_{SVV} = 0.3$ independently of n . The results obtained with the new calibrated value $(C_{SVV}, n) = (0.3, 6)$ are shown in figure 20 together with those given by the VMS-Smag model with the parameters calibrated for TGV and a reference DNS performed on a 256^3 grid. The figure shows the time history of enstrophy normalized with initial enstrophy at $Re_\lambda = 140$ and 210 and for three different resolutions, $N_{LES} = 16, 32$ and 96 . As for the TGV case, the no-model simulations overestimate the enstrophy, except for the highest resolution and the lowest Reynolds number considered, where the cutoff scale is closer to Kolmogorov scale. Both models give results in good agreement with the DNS for all Re and resolutions, with VMS-Smag being slightly more diffusive. Figure 21 compares the kinetic energy spectra obtained at $t = 1$ for the different Re and LES resolutions considered. The no-model simulation is characterized by energy pile-up at the smallest resolved scales, while the energy content of the largest ones is underestimated. This observation holds true in all cases except for the lowest Reynolds number and finer resolution, consistent with what was previously noted for enstrophy. The VMS-Smag and SVV SGS models with calibrated coefficients give spectra in good agreement with DNS up to the cut-off for all the considered Reynolds numbers and resolutions. Thus, as already observed for the TGV case, the model coefficient calibration is robust to changes in Reynolds number and resolution. However, the SVV model requires a further tuning of C_{SVV} for the HIT case. This can be explained with the method of computing artificial viscosity: in the VMS-Smag model, it is computed using the velocity field whereas in the SVV model, it depends solely on the cutoff scale.

7. Concluding remarks

An extensive study of various subgrid-scale models in large-eddy simulations using a remeshed Vortex method was conducted. The considered SGS models cover different types of modeling approaches, including classical models like the Smagorinsky one, structural modeling and spectral regularization modeling. This study was motivated by the fact that the impact of closure modeling in LES with RVM has been much less explored than for classical velocity-based formulations. Furthermore, a key advantage of RVM is its low diffusivity, facilitated by the Lagrangian treatment of the advection step. It is crucial that the adopted subgrid-scale model does not compromise this feature.

We first evaluated various subgrid scale models for the TGV benchmark at $Re = 5000$. We first considered the standard and dynamic Smagorinsky models as well as a clipped gradient model. They were found to be over-dissipative in the small scales and not enough in the large scales. In contrast, the VMS approach, which introduces the SGS viscosity only in the smallest scales of the resolved field, turned out to be well adapted to the present RVM method employing vorticity as the main variable. Finally, we appraised the SVV model, which, to the author's knowledge has never been explored within RVM. It was also found to be well suited, thanks to its multiscale nature as well as its easy integration in a fractional step algorithm already including spectral operators, making it a very low-cost approach.

Then, based on accuracy and computational cost considerations, the VMS-Smag and SVV models were selected for a further study of their sensitivity to parameters that must be a-priori assigned, i.e. model coefficients regulating the amount of introduced SGS viscosity, C_S and C_{SVV} , and filter order. This analysis was conducted again for TGV at $Re = 5000$ by using polynomial chaos expansion, that gives continuous response surfaces for the quantities of interest in the parameter space with a limited number of simulations. A remarkable variability of the results was observed, with C_S and C_{SVV} having the greatest impact, while the sensitivity to the filter used being relatively less important. Thanks to the response surfaces of the error respect to reference DNS data, "optimal" values of the parameters, in particular of C_S and C_{SVV} , could be identified for each SGS model. The so calibrated coefficients were then tested in LES of TGV and of decaying HIT, for different Reynolds numbers and grid resolutions. For the VMS-Smag model, the value of C_S calibrated for the TGV case yielded accurate results also for decaying HIT,

while recalibration of C_{SVV} was needed for the SVV model in LES of the decaying HIT. For both SGS models and flow configurations, the parameter calibration is robust to changes in the flow regime (Reynolds number) and LES grid resolution.

Summarizing, the Variational Multi-Scale Smagorinsky and the Spectral Vanishing Viscosity SGS models appear well-suited for LES with the remeshed Vortex method. This is attributed to their low computational cost and the fact that SGS viscosity is introduced only in the smallest resolved scales of the vorticity. As for the sensitivity to model parameters, it is dominated by the value of the coefficient regulating the amount of introduced SGS viscosity. This, together with the stochastic polynomial chaos expansion approach, simplifies the parameter calibration against DNS reference data. This calibration is robust to changes in Reynolds numbers and LES grid resolution, and, for the VMS-Smag model, also for a different flow configuration.

Future works will focus on the application of the present RVM approach to LES simulations of wall-bounded flows. It will be interesting to check whether the conclusions of the present SGS modeling assessment and calibration hold in presence of solid walls.

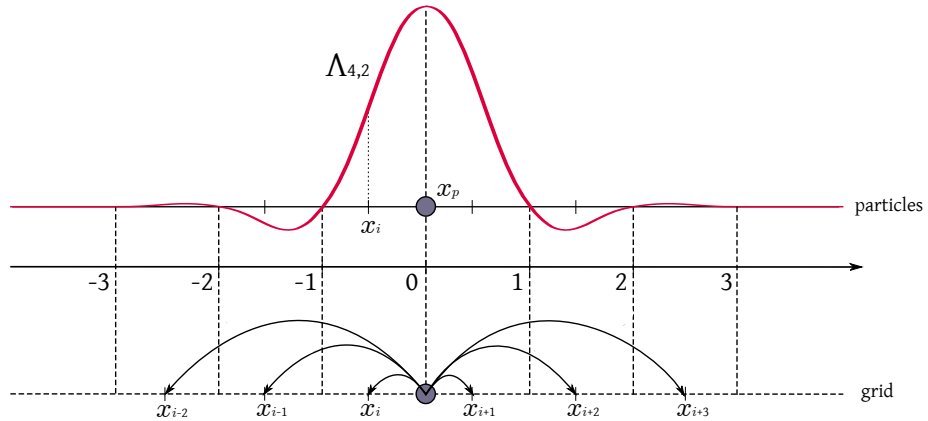


Figure 1: 1D particle remeshing with kernel $\Lambda_{4,2}$ (see eq. (2.6)).

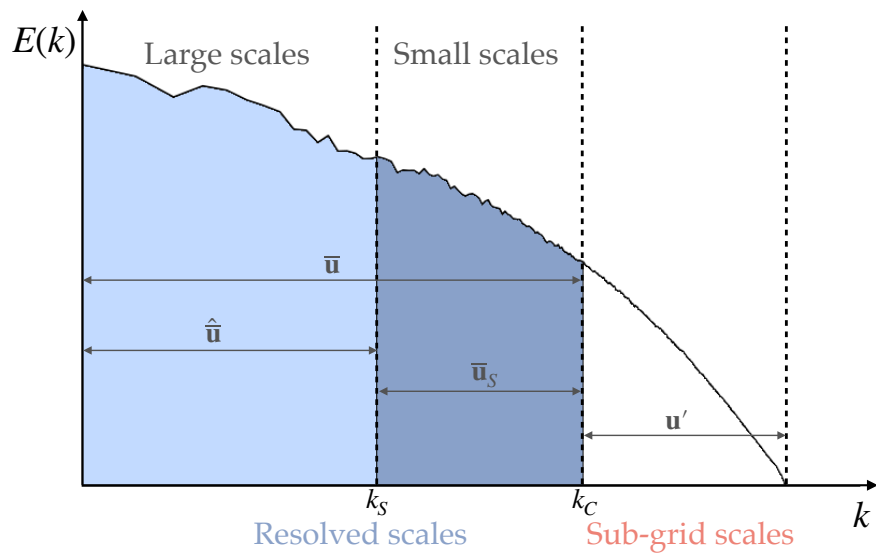


Figure 2: Filtering the smallest of the resolved scales in the VMS approach.

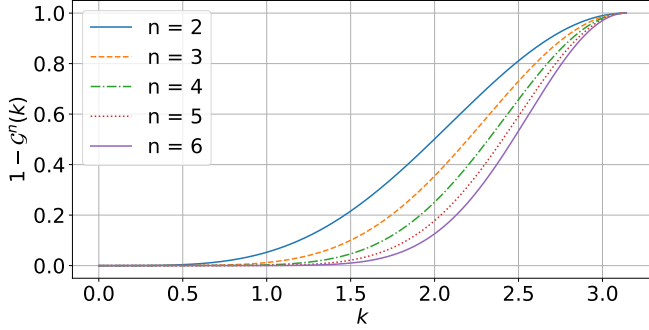


Figure 3: Explicit filtering. Plot of $(1 - \mathcal{G}^n)$ with respect to k for different values of n .

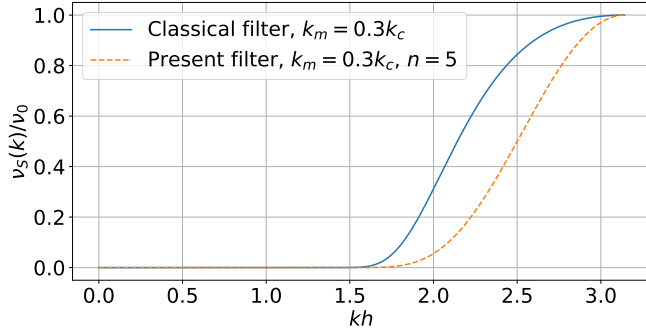


Figure 4: Evolution of the spectral artificial viscosity with respect to the wavenumber (eqs. (3.22) and (3.23)).

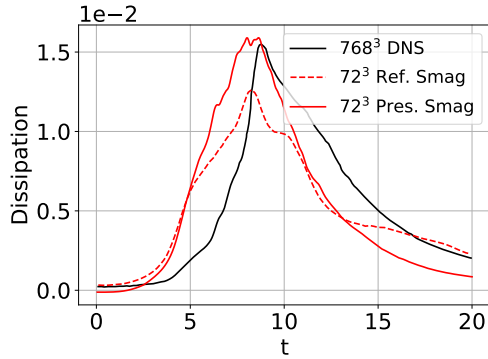


Figure 5: Comparison of standard Smagorinsky simulation from the present RVM approach with a standard Smagorinsky simulation from [61]: time history of kinetic energy dissipation for TGV at $Re = 5000$ and $N_{LES} = 72$, comparison with filtered 768^3 DNS.

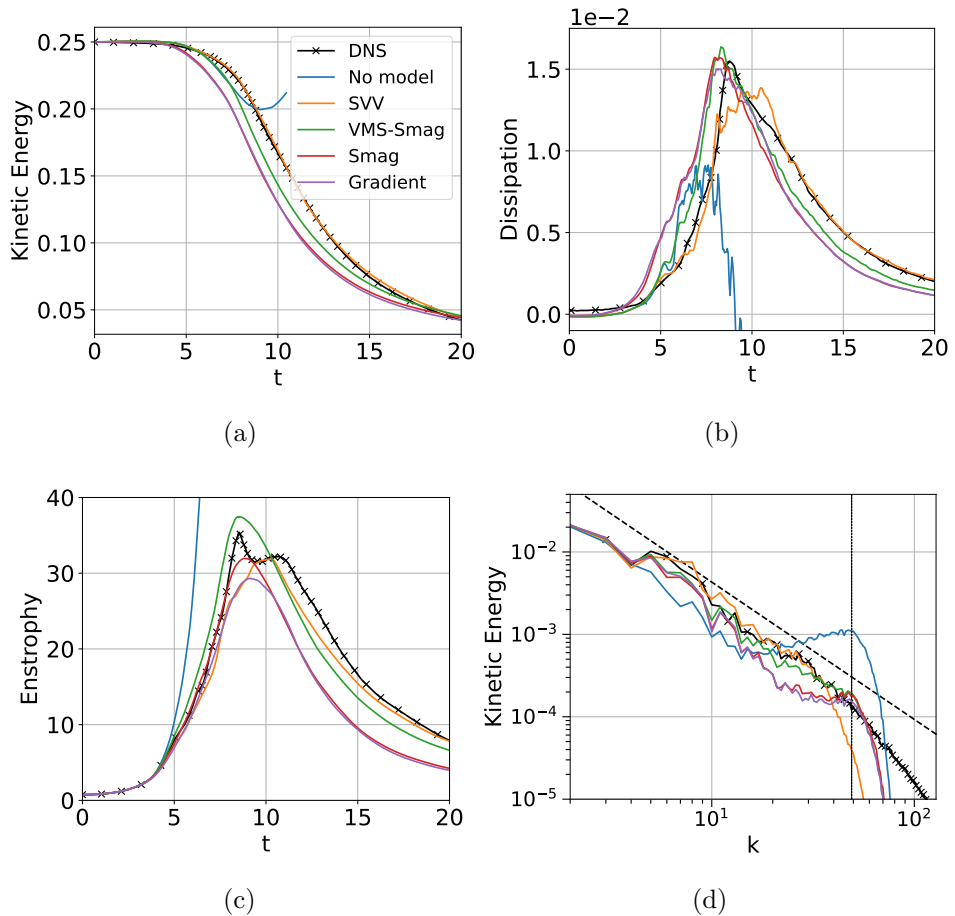


Figure 6: Time history of (a) kinetic energy, (b) kinetic energy dissipation, (c) enstrophy and (d) kinetic energy spectrum at $t = 8.5$ for the TGV with $Re = 5000$ and $N_{LES} = 96$. Comparison with 768^3 DNS for (a), (c) and (d) (filtered for (a) and (c)), and with non-filtered reference 1280^3 DNS from [33] for (b).

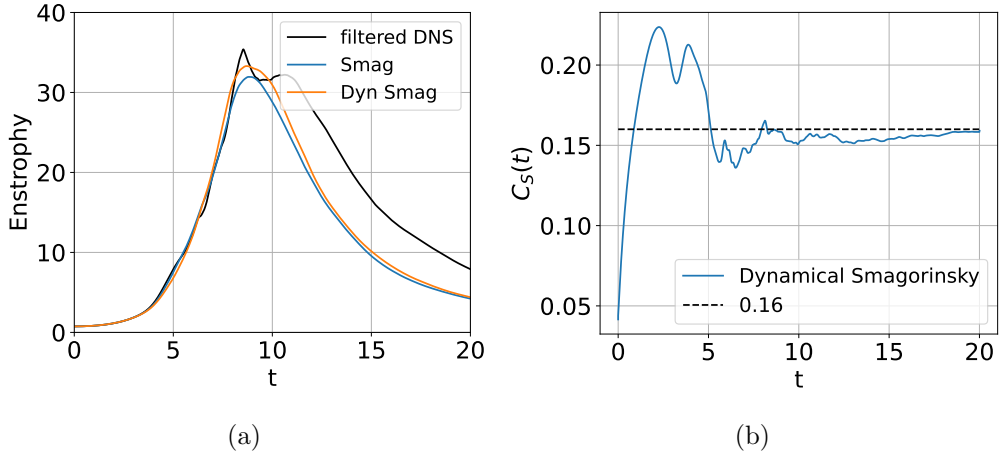


Figure 7: Comparison of standard Smagorinsky and dynamical Smagorinsky in the present RVM approach for TGV at $Re = 5000$ and $N_{LES} = 96$: (a) time history of enstrophy, comparison with filtered 768^3 DNS, (b) time history of dynamical Smagorinsky coefficient, comparison with constant standard Smagorinsky coefficient.

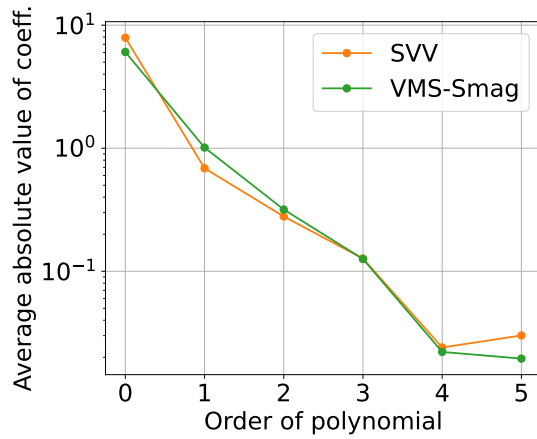


Figure 8: Average absolute value of polynomial coefficients with the order of the polynomial, evaluated over 120 surfaces responses in the uncertainty quantification for the SVV and VMS-Smag models.

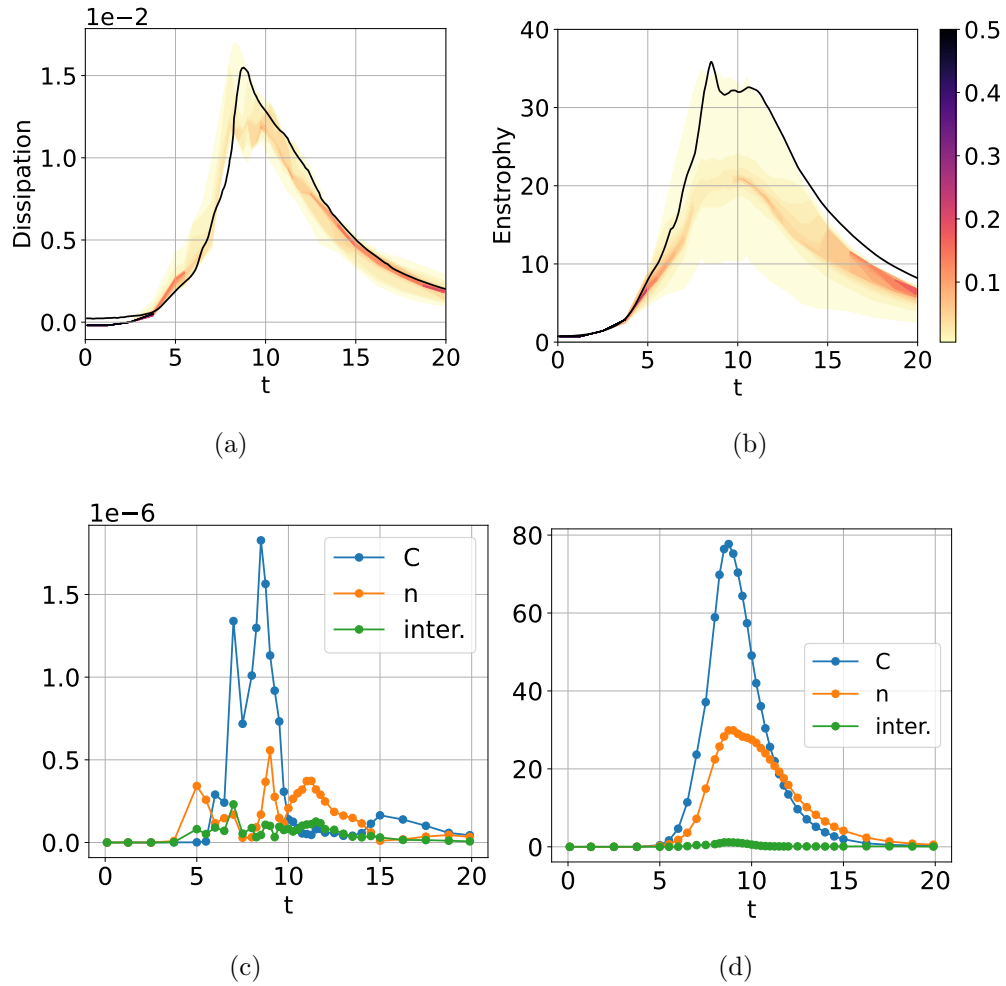


Figure 9: Sensitivity analysis of the VMS-Smag model for the TGV test case at $Re = 5000$ with $N_{LES} = 96$. (a)-(b) Probability density functions and (c)-(d) partial variances (for C_S , n , and their interaction) for time history of (left) kinetic energy dissipation and (right) enstrophy. Comparison with a reference DNS (solid black curve): (a) non-filtered 1280^3 DNS from [33], (b) filtered 768^3 DNS.

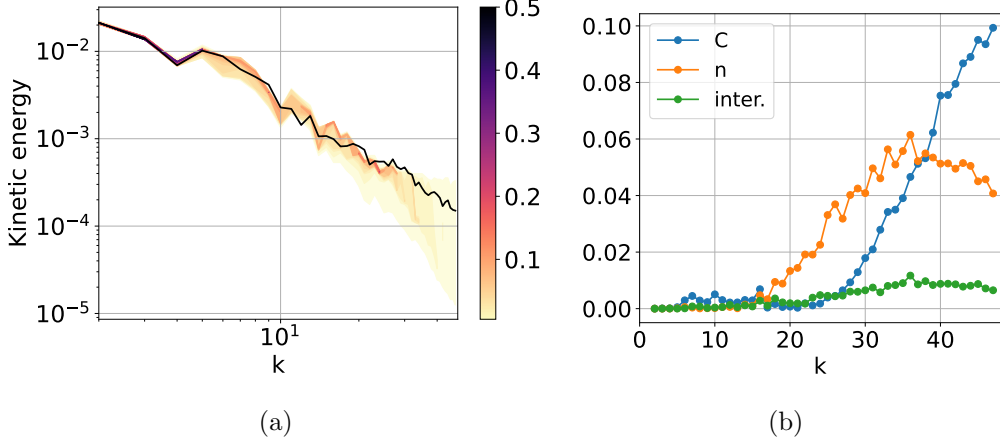


Figure 10: (a) Probability density functions and (b) partial variances (for C_S , n , and their interaction) for kinetic energy spectrum at $t = 8.5$ for VMS-Smag simulations of TGV with $Re = 5000$ and $N_{LES} = 96$. Comparison with the present reference 768^3 DNS (solid black curve).

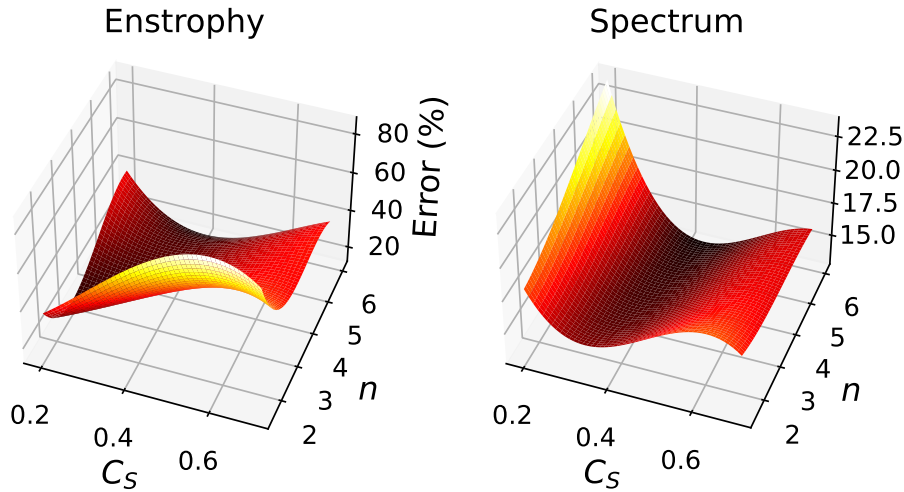


Figure 11: Surface response for the ℓ^2 -error for time history of (left) enstrophy and (right) kinetic energy spectrum at $t = 8.5$ for VMS-Smag simulations of TGV with $Re = 5000$ and $N_{LES} = 96$.

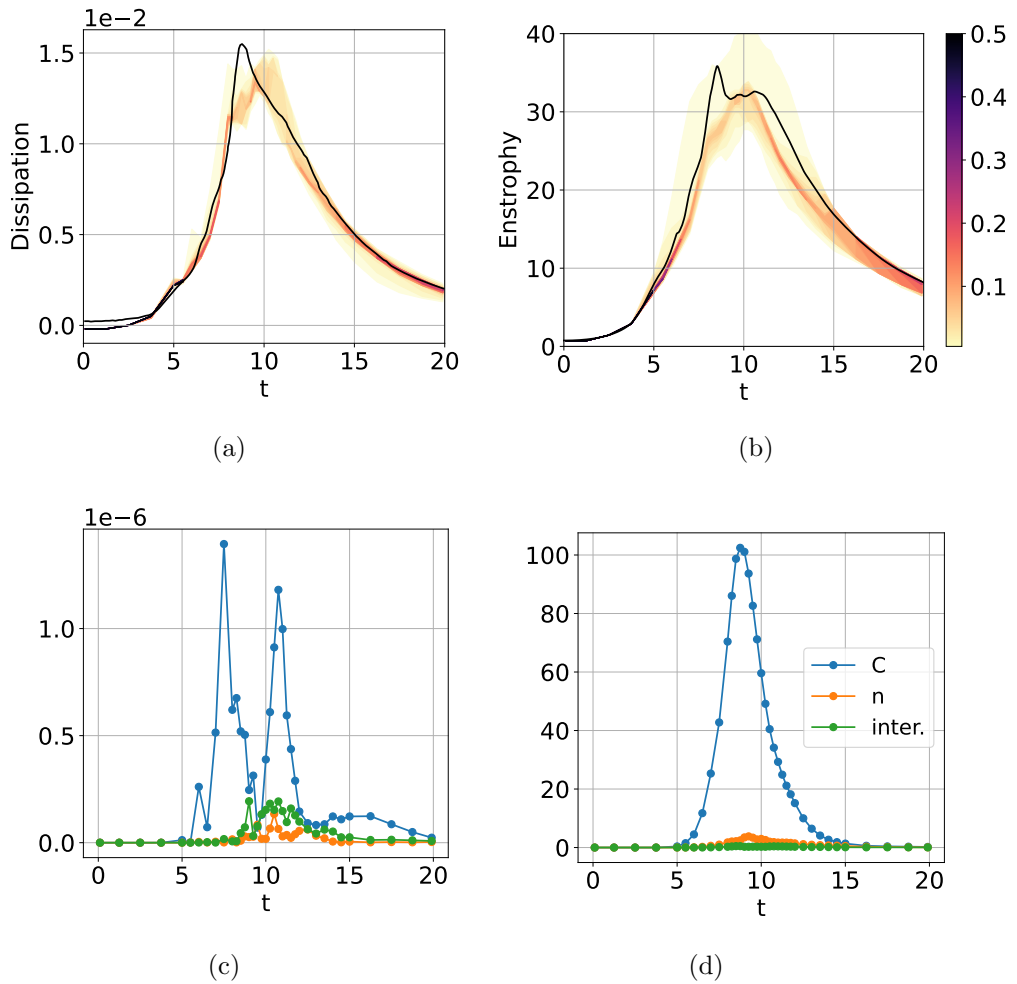


Figure 12: Sensitivity analysis of the SVV model on the TGV test case at $Re = 5000$ with $N_{LES} = 96$. (a)-(b) Probability density functions and (c)-(d) partial variances (for C_{SVV} , n , and their interaction) for time history of (left) kinetic energy dissipation and (right) enstrophy. Comparison with a reference DNS (solid black curve): (a) non-filtered 1280^3 DNS from [33], (b) filtered 768^3 DNS.

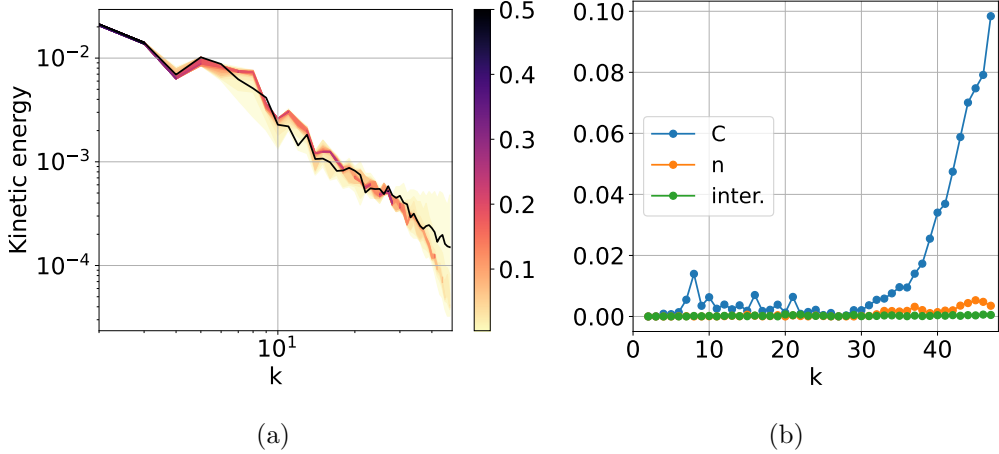


Figure 13: (a) Probability density functions and (b) partial variances (for C_{SVV} , n , and their interaction) for kinetic energy spectrum at $t = 8.5$ for SVV simulations of TGV with $Re = 5000$ and $N_{LES} = 96$. Comparison with the present reference 768^3 DNS (solid black curve).

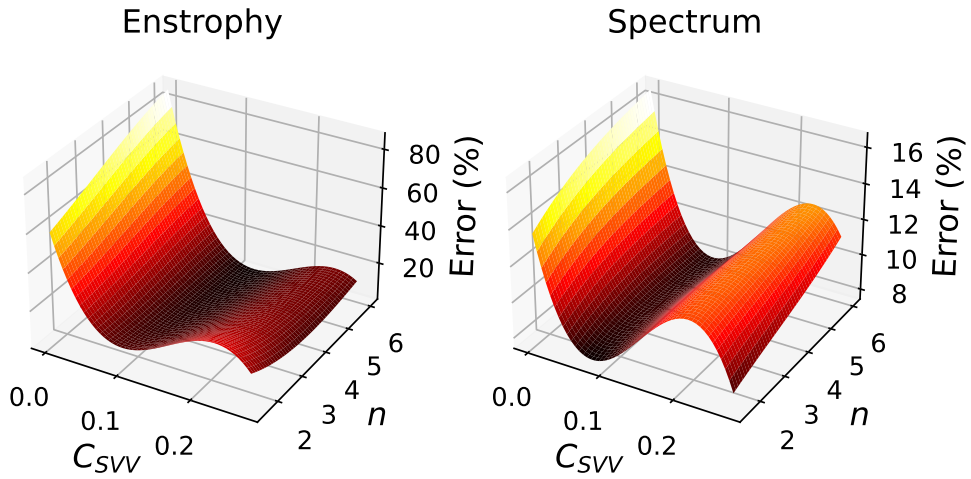


Figure 14: Surface response for the ℓ^2 -error for time history of (left) enstrophy and (right) kinetic energy spectrum at $t = 8.5$ for SVV simulations of TGV with $Re = 5000$ and $N_{LES} = 96$.

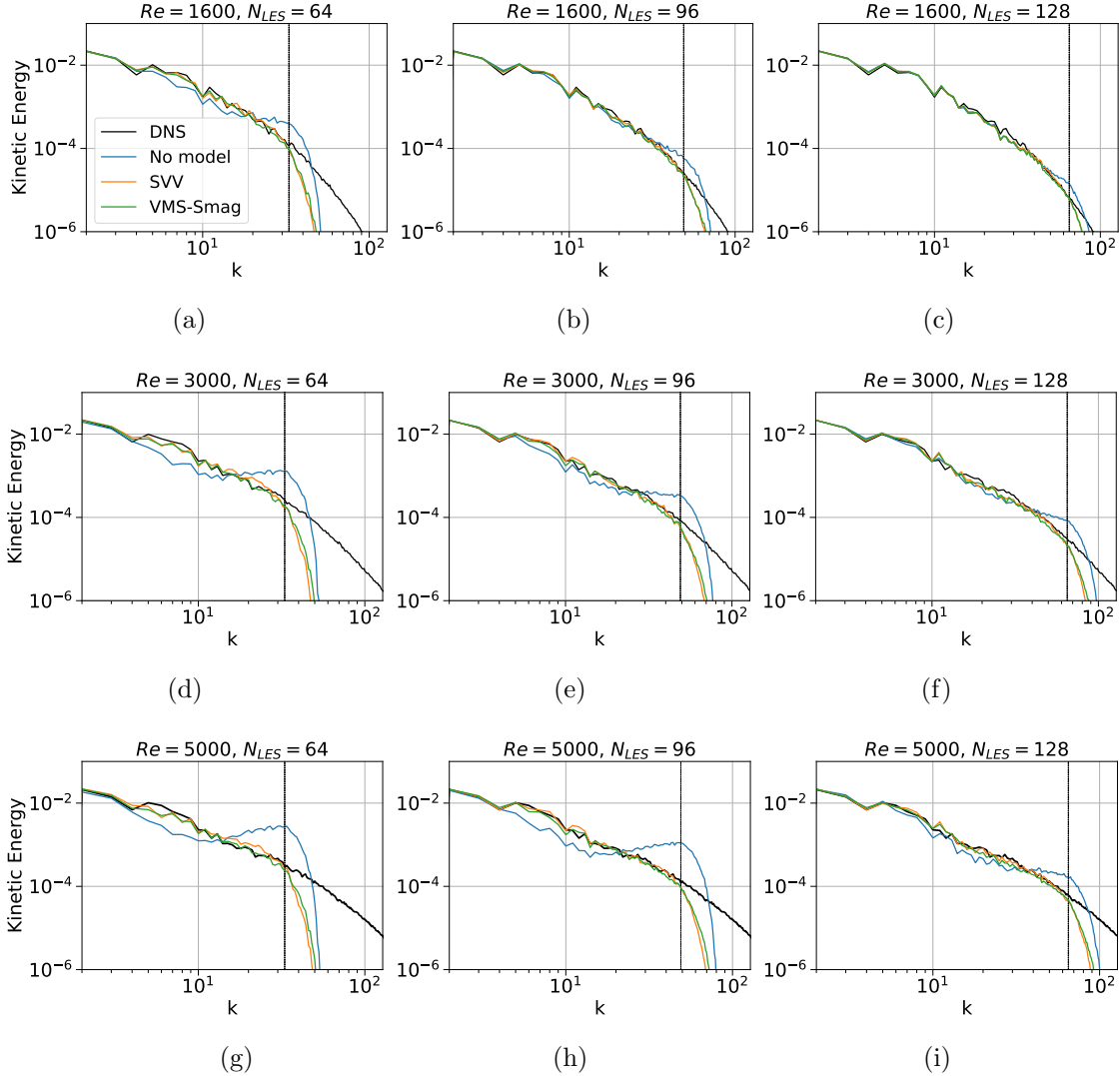


Figure 15: Kinetic energy spectrum at $t = 8.5$ for TGV, comparison with (a)-(c) 512^3 DNS, (d)-(i) 768^3 DNS. Uncertainty quantification was performed on case (h).

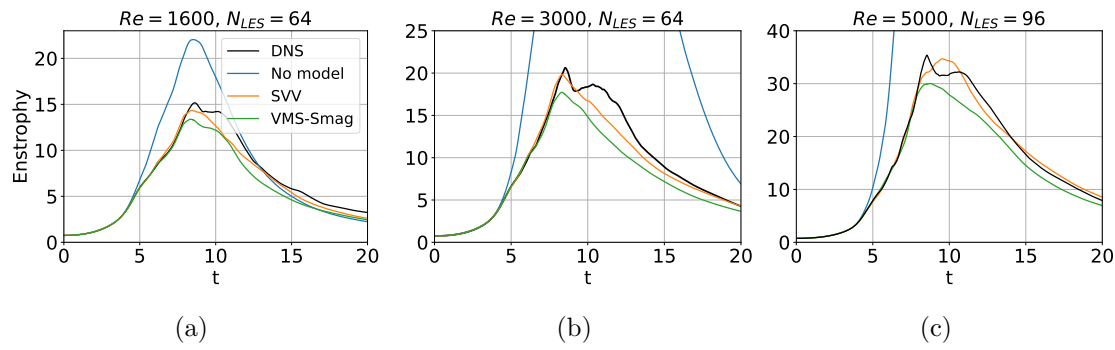


Figure 16: Time history of enstrophy for TGV at (a) $Re = 1600$, (b) $Re = 3000$ and (c) $Re = 5000$, comparison with filtered (a) 512^3 DNS, (b) and (c) 768^3 DNS. Uncertainty quantification was performed on case (c).

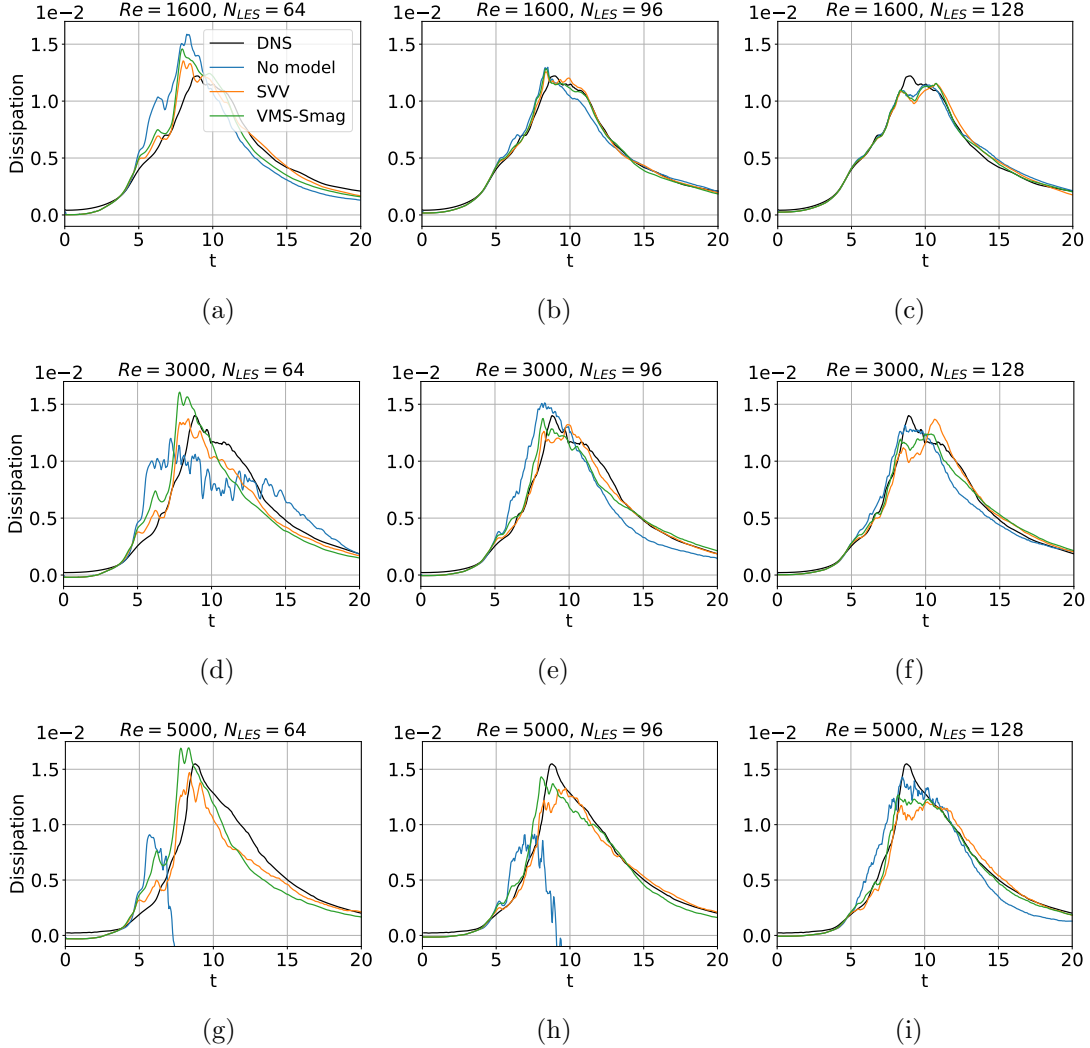


Figure 17: Time history of kinetic energy dissipation for TGV, comparison with (a)-(c) 512^3 DNS, (d)-(f) 768^3 DNS, and (g)-(i) reference 1280^3 DNS from [33]. Uncertainty quantification was performed on case (h).

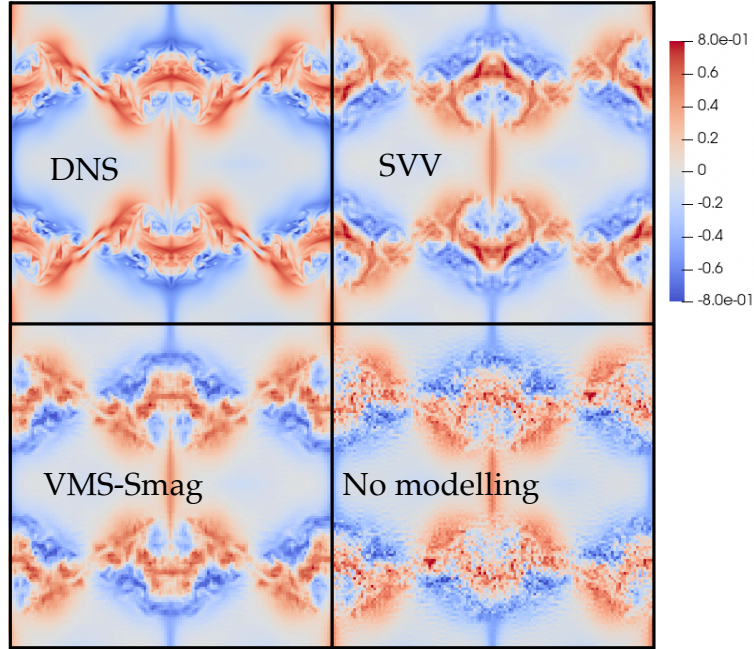


Figure 18: Qualitative comparison of the performance of the models on the flow structure depicted by the u_x velocity component at the slice $x = \pi/8$ for TGV at $Re = 5000$ and at $t = 8.5$. The no-model case, the SVV and the VMS-Smag results obtained with a $N_{LES} = 128$ resolution are compared to the DNS result with $N_{DNS} = 768$.

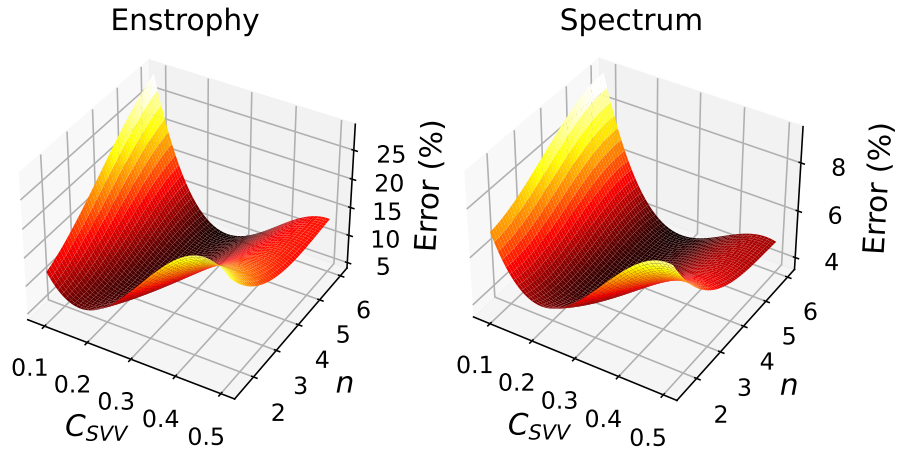


Figure 19: Surface response for the ℓ^2 -error for (left) time history of enstrophy (right) and kinetic energy spectrum at $t = 1$ for SVV simulation of decaying HIT.

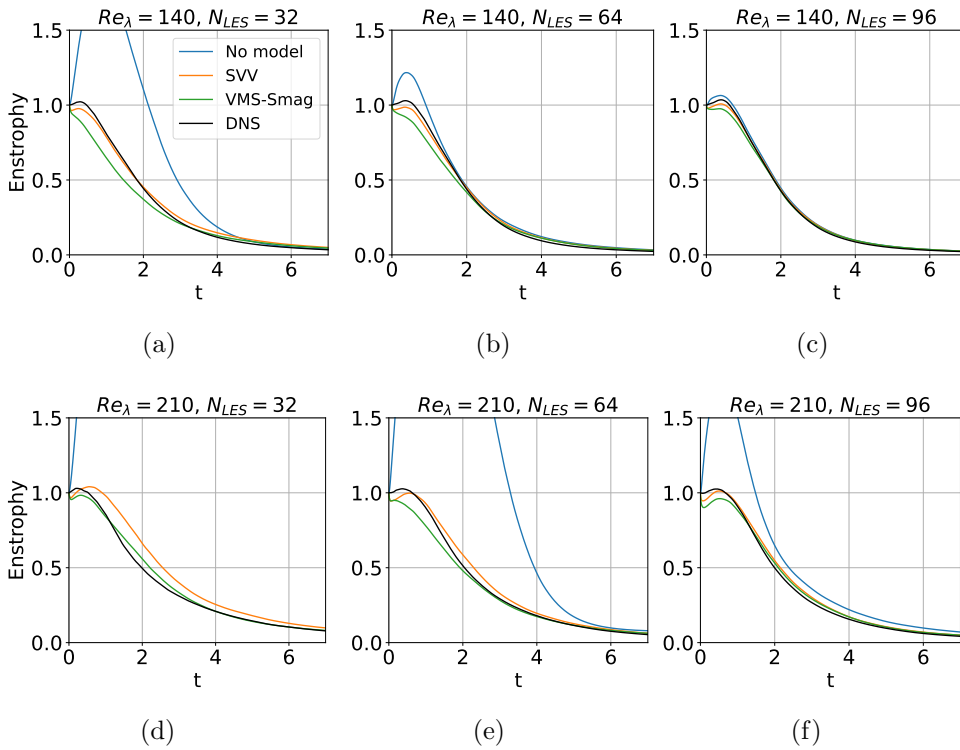


Figure 20: Time history of normalized enstrophy for the decay of HIT, comparison with filtered 256^3 DNS. Uncertainty quantification was performed on case (e).

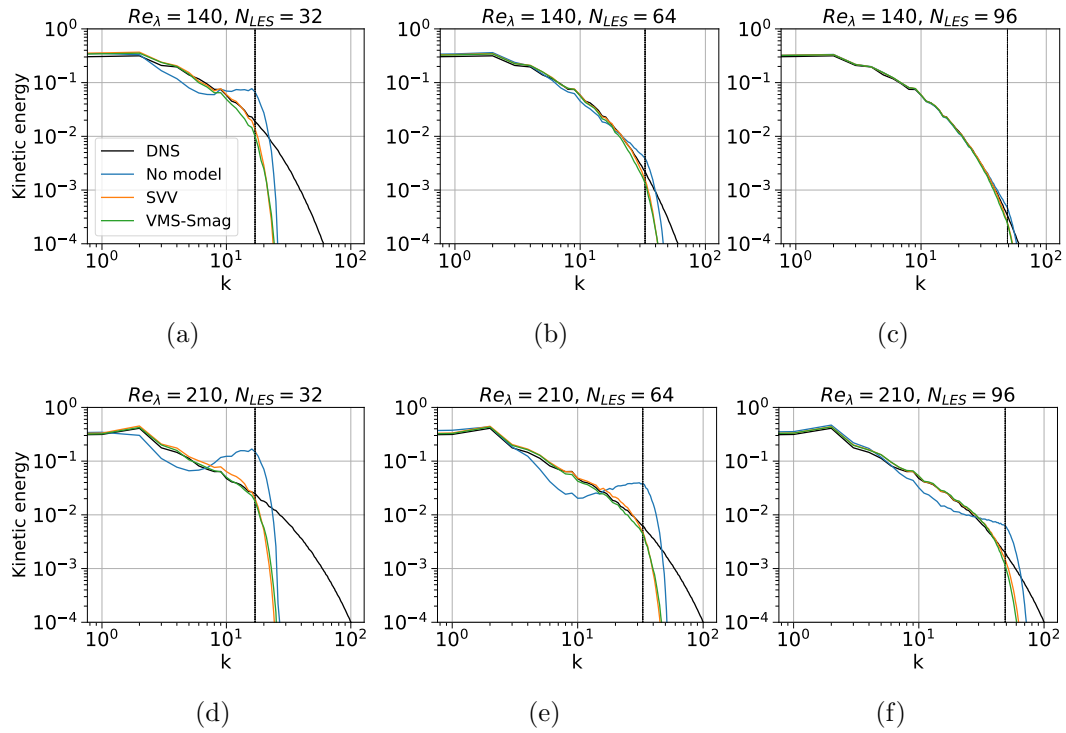


Figure 21: Kinetic energy spectrum at $t = 1$ for the decay of HIT, comparison with 256^3 DNS. Uncertainty quantification was performed on case (e).

References

- [1] G.-H. Cottet and P. D. Koumoutsakos, *Vortex Methods: Theory and Practice*. Cambridge University Press, 2000.
- [2] C. Mimeau and I. Mortazavi, “A review of vortex methods and their applications: From creation to recent advances,” *Fluids*, vol. 6, p. 68, 2021.
- [3] P. Koumoutsakos and A. Leonard, “High-resolution simulations of the flow around an impulsively started cylinder using vortex methods,” *Journal of Fluid Mechanics*, vol. 296, pp. 1–38, 1995.
- [4] G.-H. Cottet and P. Poncet, “Advances in direct numerical simulations of 3d wall-bounded flows by vortex-in-cell methods,” *Journal of Computational Physics*, vol. 193, no. 1, pp. 136–158, 2004.
- [5] C. Mimeau, S. Marié, and I. Mortazavi, “A comparison of semi-lagrangian vortex method and lattice boltzmann method for incompressible flows,” *Computers & Fluids*, vol. 224, p. 104946, 2021.
- [6] W. M. van Rees, A. Leonard, D. I. Pullin, and P. Koumoutsakos, “A comparison of vortex and pseudo-spectral methods for the simulation of periodic vortical flows at high reynolds numbers,” *J. Comput. Phys.*, vol. 230, pp. 2794–2805, 2011.
- [7] J.-B. Keck, *Numerical modelling and High Performance Computing for sediment flows*. Theses, Université Grenoble Alpes, Dec. 2019.
- [8] C. Tenaud, S. Pellerin, A. Dulieu, and L. Ta Phuoc, “Large eddy simulations of a spatially developing incompressible 3d mixing layer using the $v-\omega$ formulation,” *Computers & Fluids*, vol. 34, no. 1, pp. 67–96, 2005.
- [9] G. R. Whitehouse and A. H. Boschitsch, “Investigation of grid-based vorticity-velocity large eddy simulation off-body solvers for application to overset CFD,” *Computers & Fluids*, vol. 225, p. 104978, July 2021.
- [10] P. Sagaut, *Large Eddy Simulation for Incompressible Flows: An Introduction*. Springer Science & Business Media, 2006.
- [11] J. Smagorinsky, “General circulation experiments with the primitive equations: I. the basic experiment,” *Monthly Weather Review*, vol. 91, no. 3, pp. 99 – 164, 1963.
- [12] A. Vela-Martín, “Subgrid-scale models of isotropic turbulence need not produce energy backscatter,” *Journal of Fluid Mechanics*, vol. 937, Apr. 2022.
- [13] M. Germano, U. Piomelli, P. Moin, and W. H. Cabot, “A dynamic subgrid-scale eddy viscosity model,” *Physics of Fluids A: Fluid Dynamics*, vol. 3, no. 7, pp. 1760–1765, 1991.

- [14] T. J. R. Hughes, L. Mazzei, A. A. Oberai, and A. A. Wray, “The multiscale formulation of large eddy simulation: Decay of homogeneous isotropic turbulence,” *Physics of Fluids*, vol. 13, no. 2, pp. 505–512, 2001.
- [15] A. Vreman, *Direct and Large-Eddy Simulation of the Compressible Turbulent Mixing Layer*. PhD thesis, University of Twente, Netherlands, Dec. 1995.
- [16] Y. Zang, R. L. Street, and J. R. Koseff, “A dynamic mixed subgrid-scale model and its application to turbulent recirculating flows,” *Physics of Fluids A: Fluid Dynamics*, vol. 5, pp. 3186–3196, Dec. 1993.
- [17] R. A. Clark, J. H. Ferziger, and W. C. Reynolds, “Evaluation of subgrid-scale models using an accurately simulated turbulent flow,” *Journal of Fluid Mechanics*, vol. 91, pp. 1–16, Mar. 1979. Publisher: Cambridge University Press.
- [18] Y. Fabre and G. Balarac, “Development of a new dynamic procedure for the Clark model of the subgrid-scale scalar flux using the concept of optimal estimator,” *Physics of Fluids*, vol. 23, p. 115103, Nov. 2011.
- [19] H. Lu and F. Porté-Agel, “A modulated gradient model for scalar transport in large-eddy simulation of the atmospheric boundary layer,” *Physics of Fluids*, vol. 25, p. 015110, Jan. 2013.
- [20] A. Vollant, G. Balarac, and C. E. Corre, “A dynamic regularized gradient model of the subgrid-scale stress tensor for large-eddy simulation,” *Physics of Fluids*, vol. 28, no. 2, p. 025114, 2016.
- [21] D. K. Lilly, “A proposed modification of the germano subgrid-scale closure method,” *Physics of Fluids*, vol. 4, pp. 633–635, 1992.
- [22] E. Tadmor, “Convergence of Spectral Methods for Nonlinear Conservation Laws,” *SIAM Journal on Numerical Analysis*, vol. 26, pp. 30–44, Feb. 1989.
- [23] Y. Maday and E. Tadmor, “Analysis of the Spectral Vanishing Viscosity Method for Periodic Conservation Laws,” *SIAM Journal on Numerical Analysis*, vol. 26, pp. 854–870, Aug. 1989.
- [24] Y. Maday, S. M. O. Kaber, and E. Tadmor, “Legendre Pseudospectral Viscosity Method for Nonlinear Conservation Laws,” *SIAM Journal on Numerical Analysis*, vol. 30, pp. 321–342, Apr. 1993.
- [25] G.-S. Karamanos and G. Karniadakis, “A Spectral Vanishing Viscosity Method for Large-Eddy Simulations,” *Journal of Computational Physics*, vol. 163, pp. 22–50, Sept. 2000.
- [26] R. M. Kirby and G. E. Karniadakis, “Coarse Resolution Turbulence Simulations With Spectral Vanishing Viscosity—Large-Eddy Simulations (SVV-LES),” *Journal of Fluids Engineering*, vol. 124, pp. 886–891, Dec. 2002.

- [27] R. M. Kirby and S. J. Sherwin, “Stabilisation of spectral/hp element methods through spectral vanishing viscosity: Application to fluid mechanics modelling,” *Computer Methods in Applied Mechanics and Engineering*, vol. 195, pp. 3128–3144, Apr. 2006.
- [28] R. Pasquetti, “Spectral Vanishing Viscosity Method for Large-Eddy Simulation of Turbulent Flows,” *Journal of Scientific Computing*, vol. 27, pp. 365–375, June 2006.
- [29] R. Pasquetti, “Spectral vanishing viscosity method for LES: sensitivity to the SVV control parameters,” *Journal of Turbulence*, vol. 6, p. N12, Jan. 2005.
- [30] R. Wang, F. Wu, H. Xu, and S. J. Sherwin, “Implicit large-eddy simulations of turbulent flow in a channel via spectral/ *hp* element methods,” *Physics of Fluids*, vol. 33, p. 035130, Mar. 2021.
- [31] R. A. S. Frantz, G. Deskos, S. Laizet, and J. H. Silvestrini, “High-fidelity simulations of gravity currents using a high-order finite-difference spectral vanishing viscosity approach,” *Computers & Fluids*, vol. 221, p. 104902, May 2021.
- [32] R. Vicente Cruz and E. Lamballais, “Physical/numerical duality of explicit/implicit subgrid-scale modelling,” *Journal of Turbulence*, pp. 1–45, 2023.
- [33] T. Dairay, E. Lamballais, S. Laizet, and J. Vassilicos, “Numerical dissipation vs. subgrid-scale modelling for large eddy simulation,” *Journal of Computational Physics*, vol. 337, Feb. 2017.
- [34] E. Lamballais, R. Vicente Cruz, and R. Perrin, “Viscous and hyperviscous filtering for direct and large-eddy simulation,” *Journal of Computational Physics*, vol. 431, p. 110115, Apr. 2021.
- [35] G. S. Winckelmans, “Some Progress in Large-Eddy Simulation using the 3-D Vortex Particle Method,” in *Center for Turbulence Research Annual Research Briefs: 1995*, Dec. 1995.
- [36] G. S. Winckelmans, T. S. Lund, D. Carati, and A. A. Wray, “A priori testing of subgrid-scale models for the velocity-pressure and vorticity-velocity formulations,” in *Summer Program, Center for Turbulence Research, Stanford University and NASA Ames*, pp. 309–328, Dec. 1996.
- [37] J. R. Mansfield, O. M. Knio, and C. Meneveau, “A Dynamic LES Scheme for the Vorticity Transport Equation: Formulation and a Priori Tests,” *Journal of Computational Physics*, vol. 145, pp. 693–730, Sept. 1998.
- [38] J. Mansfield, O. Knio, and C. Meneveau, “Dynamic les of colliding vortex rings using a 3d vortex method,” *Journal of Computational Physics*, vol. 152, pp. 305–345, June 1999.

- [39] S. Ghosal, T. S. Lund, P. Moin, and K. Akselvoll, “A dynamic localization model for large-eddy simulation of turbulent flows,” *Journal of Fluid Mechanics*, vol. 286, p. 229–255, 1995.
- [40] G.-H. Cottet, “Artificial viscosity models for vortex and particle methods,” *Journal of Computational Physics*, vol. 127, no. 2, pp. 299–308, 1996.
- [41] G.-H. Cottet, D. Jiroveanu, and B. Michaux, “Vorticity dynamics and turbulence models for large-eddy simulations,” *ESAIM: Mathematical Modelling and Numerical Analysis*, vol. 37, no. 1, p. 187–207, 2003.
- [42] R. A. Clark, J. H. Ferziger, and W. C. Reynolds, “Evaluation of subgrid-scale models using an accurately simulated turbulent flow,” *Journal of Fluid Mechanics*, vol. 91, pp. 1–16, Mar. 1979.
- [43] C. Mimeau, G. H. Cottet, and I. Mortazavi, “An artificial viscosity model for 3d simulations with vortex methods,” in *10th International Conference on Computational Fluid Dynamics*, pp. 1–6, ICCFD 2018 - Proceedings, 2018.
- [44] E. J. Alvarez and A. Ning, “Reviving the Vortex Particle Method: A Stable Formulation for Meshless Large Eddy Simulation.” arXiv:2206.03658 [physics], June 2022.
- [45] N. Kornev, “Hybrid method based on embedded coupled simulation of vortex particles in grid based solution,” *Computational Particle Mechanics*, vol. 5, pp. 269 – 283, 2017.
- [46] N. Kornev and S. Samarbakhsh, “Large eddy simulation with direct resolution of subgrid motion using a grid free vortex particle method,” *International Journal of Heat and Fluid Flow*, vol. 75, pp. 86–102, 2019.
- [47] S. Samarbakhsh and N. Kornev, “Simulation of a free circular jet using the vortex particle intensified LES ($v\pi$ LES),” *International Journal of Heat and Fluid Flow*, vol. 80, p. 108489, 2019.
- [48] M. Stock, A. Gharakhani, and C. Stone, “Modeling rotor wakes with a hybrid overflow-vortex method on a gpu cluster,” 06 2010.
- [49] R. Cocco, L. Dufresne, and G. Winckelmans, “Investigation of multiscale subgrid models for les of instabilities and turbulence in wake vortex systems,” in *Complex Effects in Large Eddy Simulations*, 2007.
- [50] D.-G. Caprare, G. Winckelmans, and P. Chatelain, “An immersed lifting and dragging line model for the vortex particle-mesh method,” *Theoretical and Computational Fluid Dynamics*, vol. 34, pp. 21–48, Apr. 2020.
- [51] R. Cocco, L. Bricteux, and G. Winckelmans, “Scale dependence and asymptotic very high Reynolds number spectral behavior of multiscale subgrid models,” *Physics of Fluids*, vol. 21, p. 085101, 08 2009.

- [52] D. Xiu and G. E. Karniadakis, “The wiener–askey polynomial chaos for stochastic differential equations,” *SIAM Journal on Scientific Computing*, vol. 24, no. 2, pp. 619–644, 2002.
- [53] G. I. Taylor and A. E. Green, “Mechanism of the Production of Small Eddies from Large Ones,” *Proceedings of the Royal Society of London Series A*, vol. 158, pp. 499–521, Feb. 1937.
- [54] M. Ould-Salihi, G.-H. Cottet, and M. El Hamraoui, “Blending finite-difference and vortex methods for incompressible flow computations,” *SIAM J. Sci. Comput.*, vol. 22, pp. 1655–1674, 01 2000.
- [55] C. Mimeau, *Conception et mise en oeuvre de méthodes vortex hybrides-frontières immergées pour des milieux solides-fluide-poreux. Application au contrôle passif d'écoulements*. Theses, Université Grenoble Alpes, July 2015.
- [56] G.-H. Cottet, J.-M. Etancelin, F. Pérignon, and C. Picard, “High order Semi-Lagrangian particle methods for transport equations: numerical analysis and implementation issues,” *ESAIM: Mathematical Modelling and Numerical Analysis*, vol. 48, pp. 1029–1060, July 2014.
- [57] N. N. Mansour, J. Ferziger, and W. C. Reynolds, “Large-eddy simulation of a turbulent mixing layer,” tech. rep., Stanford University, 1978.
- [58] G. S. Winckelmans and H. Jeanmart, “Assessment of some models for les without/with explicit filtering,” in *Direct and Large-Eddy Simulation IV*, pp. 55–66, Dordrecht: Springer Netherlands, 2001.
- [59] U. Piomelli, W. H. Cabot, P. Moin, and S. Lee, “Subgrid-scale backscatter in turbulent and transitional flows,” *Physics of Fluids A: Fluid Dynamics*, vol. 3, no. 7, pp. 1766–1771, 1991.
- [60] J. Manzanero, E. Ferrer, G. Rubio, and E. Valero, “Design of a Smagorinsky spectral Vanishing Viscosity turbulence model for discontinuous Galerkin methods,” *Computers & Fluids*, vol. 200, p. 104440, Mar. 2020.
- [61] J. B. Chapelier, B. Wasistho, and C. Scalo, “A Coherent vorticity preserving eddy-viscosity correction for Large-Eddy Simulation,” *Journal of Computational Physics*, vol. 359, pp. 164–182, Apr. 2018.
- [62] V. C. B. Sousa and C. Scalo, “A unified quasi-spectral viscosity (qsv) approach to shock capturing and large-eddy simulation,” *Journal of Computational Physics*, vol. 459, p. 111139, 2022.
- [63] R. Rogallo, *Numerical Experiments in Homogeneous Turbulence*. NASA technical memorandum, National Aeronautics and Space Administration, 1981.

- [64] A. G. Lamorgese, D. A. Caughey, and S. B. Pope, “Direct numerical simulation of homogeneous turbulence with hyperviscosity,” *Physics of Fluids*, vol. 17, no. 1, p. 015106, 2005.
- [65] I. Sobol, “Global sensitivity indices for nonlinear mathematical models and their monte carlo estimates,” *Mathematics and Computers in Simulation*, vol. 55, no. 1, pp. 271–280, 2001. The Second IMACS Seminar on Monte Carlo Methods.
- [66] K. Koal, J. Stiller, and H. M. Blackburn, “Adapting the spectral vanishing viscosity method for large-eddy simulations in cylindrical configurations,” *Journal of Computational Physics*, vol. 231, pp. 3389–3405, Apr. 2012.

A. Solenoidal projection

The solenoidal reprojection step is here to ensure we always have $\nabla \cdot \boldsymbol{\omega} = 0$. Indeed, numerical errors can accumulate and to prevent that, we correct the vorticity regularly. Let us recall that any vector field can be expressed as the sum of a solenoidal (divergence-free) and an irrotational (curl-free) field. The irrotational component can be written as the gradient of a scalar potential e . Let $\boldsymbol{\omega}^*$ be the vorticity to be corrected and $\boldsymbol{\omega}$ its solenoidal part, thus the correction we seek. We write then

$$\boldsymbol{\omega}^* = \boldsymbol{\omega} + \nabla e \quad (\text{A.1})$$

then

$$\nabla \cdot \boldsymbol{\omega}^* = \nabla \cdot \boldsymbol{\omega} + \nabla \cdot \nabla e \quad (\text{A.2})$$

and since $\nabla \cdot \boldsymbol{\omega} = 0$,

$$\Delta e = \nabla \cdot \boldsymbol{\omega}^* \quad (\text{A.3})$$

and by applying the Laplacian operator to (A.1) we get

$$\Delta \boldsymbol{\omega}^* = \Delta \boldsymbol{\omega} + \nabla \Delta e \quad (\text{A.4})$$

which means $\boldsymbol{\omega}$ is solution to

$$\Delta \boldsymbol{\omega} = \Delta \boldsymbol{\omega}^* - \nabla(\nabla \cdot \boldsymbol{\omega}^*) \quad (\text{A.5})$$

which is a Poisson equation that can easily be solved in the Fourier space.

B. Proof of equivalence of (3.5) and (3.6) for incompressible fluids

Starting from

$$\mathbf{g} = -\nabla \times (\nu_{SGS} \nabla \times \boldsymbol{\omega}) \quad (\text{B.1})$$

developing the expression:

$$\begin{aligned} \mathbf{g} &= -\nu_{SGS} \nabla \times \nabla \times \boldsymbol{\omega} - \nabla \nu_{SGS} \times (\nabla \times \boldsymbol{\omega}) \\ &= -\nu_{SGS} \nabla(\nabla \cdot \boldsymbol{\omega}) + \nu_{SGS} \Delta \boldsymbol{\omega} - \nabla \nu_{SGS} \times \nabla \times \boldsymbol{\omega} \\ &= \nu_{SGS} \Delta \boldsymbol{\omega} - \nabla \nu_{SGS} \times \nabla \times \boldsymbol{\omega}. \end{aligned} \quad (\text{B.2})$$

Using Einstein's notation, summing over $j \neq i$:

$$\begin{aligned} \mathbf{g}_i &= \nu_{SGS} \partial_i^2 \boldsymbol{\omega}_i + \nu_{SGS} \partial_j^2 \boldsymbol{\omega}_i - \partial_j \nu_{SGS} (\partial_i \boldsymbol{\omega}_j - \partial_j \boldsymbol{\omega}_i) \\ &= \nu_{SGS} \partial_i^2 \boldsymbol{\omega}_i + \partial_j (\nu_{SGS} \partial_j \boldsymbol{\omega}_i) - \partial_j \nu_{SGS} \partial_j \boldsymbol{\omega}_i - \partial_j (\nu_{SGS} \partial_i \boldsymbol{\omega}_j) \\ &\quad + \nu_{SGS} \partial_i \partial_j \boldsymbol{\omega}_j + \partial_j \nu_{SGS} \partial_j \boldsymbol{\omega}_i \\ &= \nu_{SGS} \partial_i^2 \boldsymbol{\omega}_i + \partial_j (\nu_{SGS} \partial_j \boldsymbol{\omega}_i) - \partial_j (\nu_{SGS} \partial_i \boldsymbol{\omega}_j) + \nu_{SGS} \partial_i \partial_j \boldsymbol{\omega}_j \end{aligned} \quad (\text{B.3})$$

and since $\nu_{SGS} \partial_i^2 \boldsymbol{\omega}_i + \nu_{SGS} \partial_i \partial_j \boldsymbol{\omega}_j = \nu_{SGS} \partial_i (\nabla \cdot \boldsymbol{\omega}) = 0$

$$\mathbf{g}_i = \partial_j (\nu_{SGS} \partial_j \boldsymbol{\omega}_i) - \partial_j (\nu_{SGS} \partial_i \boldsymbol{\omega}_j) = \partial_j (\nu_{SGS} (\partial_j \boldsymbol{\omega}_i - \partial_i \boldsymbol{\omega}_j)) \quad (\text{B.4})$$

which is precisely the \mathbf{g}_i given by (3.6).